Supporting Information for

Rapid self-reconstruction of Fe-modified Ni hydroxysulfide for efficient and stable large-current-density water/seawater oxidation

Chuqiang Huang,[a] Qiancheng Zhou,[a] Dingshuo Duan,[a] Luo Yu,[d] Wei Zhang,[e] Zhouzhou Wang,[a] Jin Liu,[a] Bowen Peng,[a] Pengfei An,[f] Jing Zhang,[f] Liping Li,*[b] Jiaguo Yu,*[c] and Ying Yu*[a]

[a.] Institute of Nanoscience and Nanotechnology, College of Physical Science and Technology, Central China Normal University, Wuhan 430079, China. *E-mail: yuying01@mail.ccnu.edu.cn

[b.] State Key Laboratory of Inorganic Synthesis and Preparative Chemistry, College of Chemistry, Jilin University, Changchun 130012, China. *E-mail: lipingli@jlu.edu.cn

[c.] Laboratory of Solar Fuel, Faculty of Materials Science and Chemistry, China University of Geosciences, Wuhan 430079, China. *E-mail: yujiaguo93@cug.edu.cn

[d.] Department of Chemistry, The Chinese University of Hong Kong, Shatin, New Territories, Hong Kong, 999077, China.

[e.] State Key Laboratory of Advanced Technology for Materials Synthesis and Processing, Wuhan University of Technology, Wuhan 430070, China.

[f.] Beijing Synchrotron Radiation Facility, Institute of High Energy Physics, Chinese Academy of Science Institution, Beijing 100049, China.

*E-mails: yuying01@mail.ccnu.edu.cn (Y. Y.); lipingli@jlu.edu.cn (L. L.); yujiaguo93@cug.edu.cn (Y. J.).

1. Material synthesis

Chemicals. $(NH_4)_2S_2O_8$, $Na_2S_2O_3 \cdot 5H_2O$, $(NH_4)_2Fe(SO_4)_2$, $Ni(NO_3)_2 \cdot 6H_2O$, NH_4F, $(NH_2)_2CO$, $Co(NO_3)_2 \cdot 6H_2O$, NaH_2PO_2, and isopropanol were purchased from Sinopharm Chemical Reagent Co., Ltd. All of the above reagents are analytical grade. Ni foam (99.99%, thickness: 1.5 mm) and IrO_2 was purchased from Changde Liyuan New Materials Co., Ltd. and Shanghai Macklin Biochemical Co., Ltd., respectively. $H^{18}O$ (97 atom%) was purchased from Shanghai Aladdin Biochemical Technology Co., Ltd. All chemicals were used directly without further purification. Deionized water (18.3 MΩ·cm) was used for the preparation of all aqueous solutions.

Synthesis of nickel hydroxysulfide (NiSOH). NiSOH nanosheet arrays were prepared by a wet chemical oxidation method. 1.369 g $(NH_4)_2S_2O_8$ was added into 80 mL deionized water, and stirred for 10 min. 0.496 g $Na_2S_2O_3 \cdot 5H_2O$ was subsequently dissolved into the above solution, and then left to rest in ice water bath for 2 min. Then, a pre-treated Ni foam (2 x 1.5 cm^2) was immersed in the solution, which had been kept under ice water bath conditions for 10 min. After reaction, the Ni foam was washed with deionized water, dried naturally, and ultrathin NiSOH nanosheet arrays were obtained.

Synthesis of Fe-modified nickel hydroxysulfide (Fe-NiSOH). Fe-NiSOH nanosheet arrays were prepared *via* anodic oxidation process in 0.01 M $(NH_4)_2Fe(SO_4)_2$ solution, using the pre-prepared NiSOH grown on Ni foam as working electrode, Ag/AgCl electrode and carbon rod as reference electrode and counter electrode, respectively. The effective area of the working electrode was 2 cm^2. The Fe-NiSOH-x (x = 2, 5, 7, 8, 9, and 10) electrodes were obtained by anodic oxidation under constant current densities (2, 5, 7, 8, 9, and 10 mA cm^{-2}) for 20 min. The Fe-NiSOH-x min (x = 10, 15, 20, and 30) electrodes were prepared by anodic oxidation for 10, 15, 20, and 30 min under current density of 8 mA cm^{-2}, respectively. Fe-NiSOH in the whole text is represented for Fe-NiSOH-8 and Fe-NiSOH-20 min because of its relatively high OER performance, unless otherwise mentioned.

Synthesis of nickel hydroxide (Ni-OH). A pre-treated Ni foam (2 x 5 cm^2) was placed in 60 mL deionized water, including 3 mmol $Ni(NO_3)_2 \cdot 6H_2O$, 4 mmol NH_4F, and 10 mmol $(NH_2)_2CO$. After hydrothermal reaction at 120 ℃ for 6 h, Ni-OH nanosheet arrays on Ni foam was obtained.

Synthesis of Fe-modified nickel hydroxide (Fe-Ni-OH). The synthesis process of Fe-Ni-OH was similar to that of Fe-NiSOH except that Ni-OH was used as the working electrode.

Synthesis of CoP nanorod arrays on Ni foam. A pre-treated Ni foam (2 x 5 cm^2) was placed in 60 mL deionized water, including 3 mmol $Co(NO_3)_2 \cdot 6H_2O$, 4 mmol NH_4F, and 10 mmol $(NH_2)_2CO$. After hydrothermal reaction at 120 ℃ for 6 h, the Co-OH nanorod arrays on Ni foam was obtained. After drying, CoP nanorod arrays was prepared by a phosphating process under N_2 atmosphere at 350 ℃ for 2 h, where NaH_2PO_2 was placed upstream of tube furnace, and the sample downstream.

Preparation of the IrO_2 electrode: 5 mg IrO_2 and 25 μL Nafion was dispersed in 250 μL isopropanol, and ultrasonicated for 40 min. Then, the suspension was coated onto a pre-treated Ni foam, and dried in a vacuum oven for 6 h. The loading amount of the IrO_2 electrode was about 2 mg cm^{-2}.

2. Physical characterizations

The morphology structure and element amount of the electrodes were investigated by scanning electron microscope (SEM, JEOL JSM-7900) and transmission electron microscopy (TEM, JEOL 2100F) coupled with energy dispersive X-ray (EDX) spectroscopy (SEM: Oxford Ultim Max 65; TEM: QUANTAX 200-TEM). The crystal structure of the electrodes was determined *via* X-ray diffraction (XRD) pattern from an X'Pert PRO diffractometer. As a good supplement to chemical compositions of the catalysts, Raman spectrum of the electrodes were collected on HORIBA LabRAM Spectrometer with the laser of 532 nm. The surface chemical composition and oxidation states of the catalysts before and after CV activation were tested through X-ray photoelectron spectroscopy (XPS) using an ESCALAB 250XI

(Thermo) system. The electronic structures and local coordination environments of the catalysts were investigated by X-ray absorption spectroscopy (XAS), which measured in fluorescence mode at the beamline 1W2B of the Beijing Synchrotron Radiation Facility (BSRF) in China using a double crystal Si (111) monochromator. The pore size distribution and total pore area of Ni foam substrate were tested by mercury intrusion method at AutoPore Iv 9510 with the range of 0.10 to 61,000.00 psia.

3. Data analysis

The XRD data were analyzed by MDI-Jade 6.0. The XPS data were analyzed by Thermo Avantage. All XPS of the catalysts were calibrated referenced to the C 1s peak (284.8 eV for adventitious hydrocarbon). The XAS data were analyzed and fitted by using Athena (Demeter 0.9.25, an interface to IFEFFIT) and Artemis (Demeter 0.9.25).[1] All the Ni and Fe K-edge XAS raw date recorded from the beamline were calibrated by aligning the E_0 of pure metal foils (8333 eV for Ni and 7112 eV for Fe). During curve fittings, the amplitude reduction factor S_0^2 was fixed to be 0.779, which is determined from fitting the reference sample of Ni foil. No R factors exceed 0.02 in the fitting results of all curves, suggesting the good fitting quality. All Figures were drawn through Origin 2017 and Adobe PhotoShop CS6.

4. *In-situ* spectroscopic and ^{18}O isotope-labelled experiments.

In-situ Raman spectrum of the catalysts were recorded in a three-electrode system injected with 1 M KOH, as the schematic illustration shown in **Fig. 5a**. The freshly prepared catalysts were used as the working electrode, and the Hg/HgO electrode and Pt electrode were used as the reference electrode and counter electrode, respectively. The applied potential ranges from open circuit potential (OCP) to 1.515 V *vs.* RHE, in which the spectra were collected after 10 minutes of stabilization at each potential.

The *in-situ* X-ray absorption spectroscopy (XAS) data were collected in a home-made three-electrode cell injected with 1 M KOH. The freshly catalysts on Ni

foam (2 cm × 2 cm) were dispersed into 5 mL anhydrous ethanol *via* ultrasonicating for 40 minutes. Then, 30 μL of 5 % Nafion 117 solution was added to 150 μL of the above solution, ultrasonicated for 20 min. The suspension was coated onto a thin carbon paper (2 cm × 5 cm, thickness of 30 μm), and dried in vacuum. The thin carbon paper loaded with catalyst powders, connected with a slip of Cu tape, was fixed against the wall of the reaction cell as the working electrode. The catalyst layer faces inward and contacts the electrolyte through a 0.8 cm hole. The counter and reference electrodes are graphite and Hg/HgO electrode, respectively.

The freshly prepared samples were operated at a constant current density of 10 mA cm^{-2} in 1 M KOH with $H_2{}^{18}O$ as water source for 30 min to obtain the ^{18}O-labelled Fe-NiSOH and Fe-Ni-OH samples with ^{18}O-MOOH. *In-situ* Raman measurements of the ^{18}O-labelled samples were carried out at a constant current density of 10 mA cm^{-2} in 1 M KOH with $H_2{}^{16}O$ for different time (1 min to 30 min). Moreover, the gas products of the ^{18}O-labelled samples were collected at a constant current density of 10 mA cm^{-2} in 1 M KOH with $H_2{}^{16}O$ for 30 min. The O-isotope signals were detected by high-resolution mass spectrometer (Agilent 8890-7250 GC-QTOF).

5. Electrochemical measurements

All electrochemical measurements were performed on a CHI660 electrochemical workstation. The electrochemical characterizations of the single electrodes were carried out in a three-electrode system injected with 1 M KOH water/seawater, where graphite and Hg/HgO electrode were used as counter and reference electrode, respectively. The water-splitting performance of the electrolyzers was tested in a two-electrode system, where OER electrode are as the anode and HER electrode as the cathode. The natural seawater was collected from Xianglu Bay of Zhuhai city, Guangdong Province, China, and filtered to remove large sediment and silt. To obtain 1 M KOH seawater, 5.61 g KOH was dissolved in 100 mL seawater. After standing, the supernatant was taken as electrolyte solution with a pH of about 13.8. To avoid

the influence of redox reaction of catalyst, the catalytic activity was determined by reverse linear sweep voltammetry (LSV) curves (from positive to negative direction) at a scan rate of 2 mV s^{-1} with 90% IR correction. The double-layer capacitance values were obtained *via* CV curves with the scan rates of 50-100 mV s^{-1}. Electrochemical impedance spectroscopy (EIS) of the single electrodes was examined from 1000 kHz to 1.0 Hz with the overpotential of 310 mV. All the potentials for the single electrodes were converted through Nernst equation ($E_{RHE} = E_{Hg/HgO} + 0.0591pH + 0.098$). The oxygen faradic efficiency (FE) of gaseous product was determined in a H-type electrolytic cell at constant current densities by a gas chromatography (GC-2014, Shimadzu, Japan). The Fe-NiSOH-CV and Fe-Ni-OH-CV represent the Fe-NiSOH and Fe-Ni-OH electrode after 20 CVs with the potential region from 1.115 to 1.615 V *vs.* RHE at the scan rate of 50 mV s^{-1}, respectively.

6. DFT calculations

All the calculations were performed by using Vienna ab initio program package (VASP).[2] The exchange and correlation effects of the electrons were described by using the Perdew-Burke-Ernzerhof[3] (PBE) functional of a generalized gradient approximation (GGA) method.[4] The projector augmented wave (PAW) method was used to describe the electron-ion interaction and spin polarization was considered. The cutoff energy of the plane-wave was set as 500 eV. The (2×3×3) k-point mesh was used for k-space integration in our structure relaxations. The (4×6×6) k-point mesh was used for electronic structure calculation. Conjugate-gradient algorithm was used to relax the ions into their instantaneous ground state. The structure involved were fully relaxed with the energy and force convergences less than 1×10^{-6} eV and 0.02 eV $Å^{-1}$, respectively. As for the models shown in **Fig. S46**, 3×4×1 supercells of $Ni(OH)_2$ was built, where the lattice parameters are a = b = 3.16 Å, c = 6.68 Å. One of OH was substituted by S atom to obtain S-$Ni(OH)_2$, and the doping amount was about 2%, corresponding to the S content in the Fe-NiSOH electrodes. Three Ni atoms of S-$Ni(OH)_2$ were replaced by Fe atoms and deprotonated to gain S-$Ni(OH)_2$/FeOOH. S

atoms in the S-$Ni(OH)_2$ and S-$Ni(OH)_2$/FeOOH catalysts were further removed to form the S-leached (SL) catalysts (**Fig. S47**). During self-reconstruction of the catalysts (**Fig. S48**), pure $Ni(OH)_2$, SL S-$Ni(OH)_2$, SL S-$Ni(OH)_2$/FeOOH were optimized as original models. These models were further deprotonated to form the corresponding NiOOH, SL S-NiOOH, and SL S-NiOOH/FeOOH, respectively, to construct Ni^{3+} species. Ni^{3-4+} was established by removing one H atom for the corresponding NiOOH models. SL $NiOOH_{0.5}$/FeOOH and SL-NiOO/FeOOH models were built by removing a half number of H atoms and all H atoms of SL NiOOH/FeOOH (**Fig. S49**). All the model structures were optimized.

7. Supplementary Figures

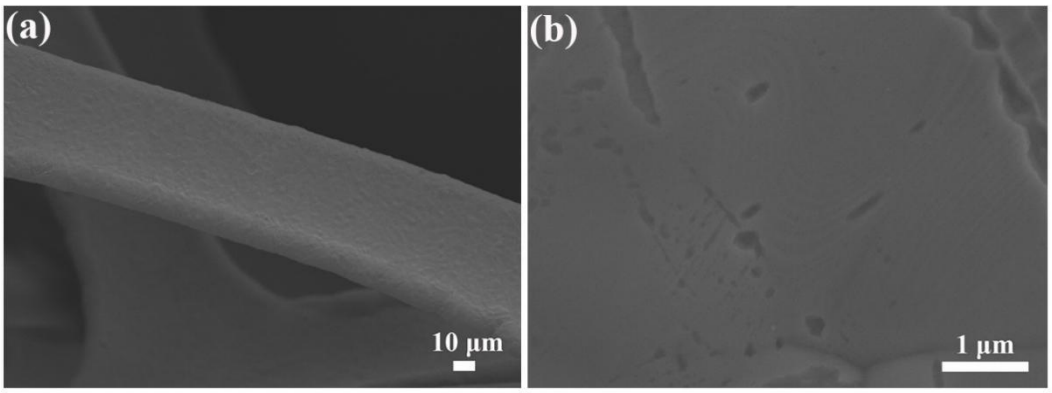

Fig. S1 SEM images of pre-treated Ni foam with different magnifications.

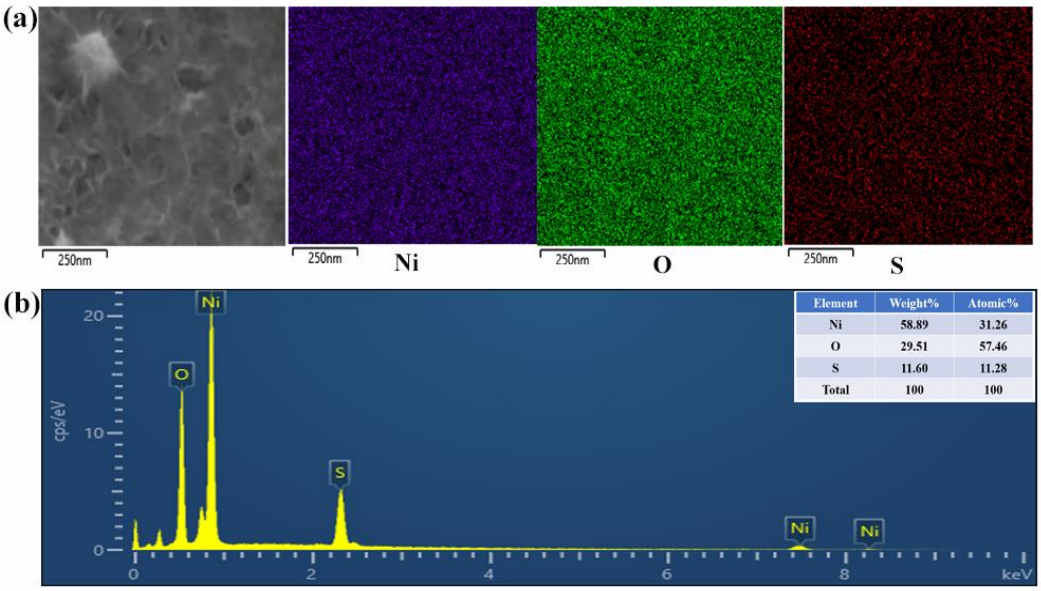

Element	Weight%	Atomic%
Ni	58.89	31.26
O	29.51	57.46
S	11.60	11.28
Total	100	100

Fig. S2 (a) SEM image with corresponding elemental mapping and (b) energy dispersive X-ray (EDX) spectrum of NiSOH electrode.

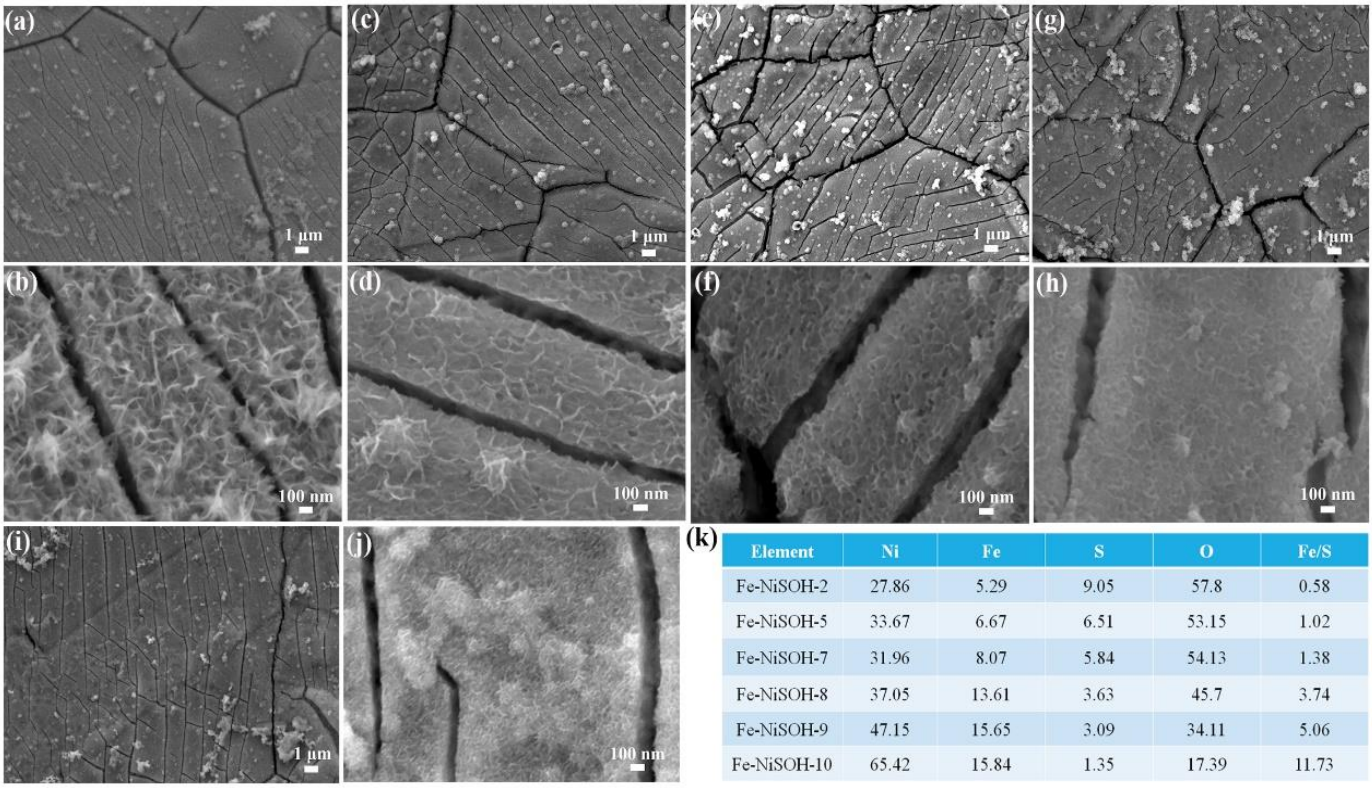

(k)

Element	Ni	Fe	S	O	Fe/S
Fe-NiSOH-2	27.86	5.29	9.05	57.8	0.58
Fe-NiSOH-5	33.67	6.67	6.51	53.15	1.02
Fe-NiSOH-7	31.96	8.07	5.84	54.13	1.38
Fe-NiSOH-8	37.05	13.61	3.63	45.7	3.74
Fe-NiSOH-9	47.15	15.65	3.09	34.11	5.06
Fe-NiSOH-10	65.42	15.84	1.35	17.39	11.73

Fig. S3 SEM images of (a-b) Fe-NiSOH-2, (c-d) Fe-NiSOH-5, (e-f) Fe-NiSOH-7, (g-h) Fe-NiSOH-9, (i-j) Fe-NiSOH-10 with different magnifications. (k) Element amount of Fe-NiSOH-x (x = 2, 5, 7, 8, 9, and 10) electrodes obtained by SEM coupled with EDX spectrum.

Combining with the morphology and composition of the Fe-NiSOH-x electrode, the anodizing process results in the incorporation of Fe into NiSOH for forming Fe-NiSOH-x accompanied by S atoms leaching, which demonstrates the morphology of many small lawns stacked by abundant nanosheets. The influence of anodizing current densities for the Fe-NiSOH-x electrodes can be qualitatively illustrated by their element amount. With the increase of anodizing current densities, the atomic amount of S gradually decreases and Fe content increases, as evidenced by the gradually increasing atomic ratio of Fe to S (Fe/S). Comparing the OER activity of these catalysts (**Fig. S22**), we can see that the optimal anodizing current density is 8 mA cm^{-2}, which mainly be due to the optimized Fe and S content for the Fe-NiSOH catalyst.

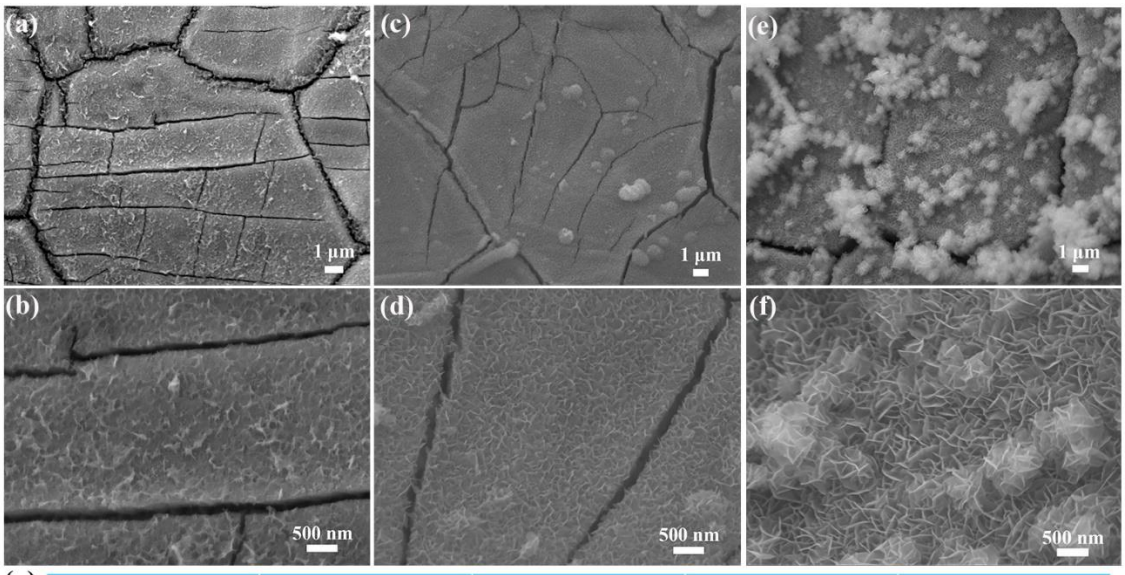

(g)

Element	Ni	Fe	S	O
10 min	37.33	4.74	7.76	50.18
15 min	32.27	7.58	3.91	56.24
20 min	37.05	13.61	3.63	45.8
30 min	46.51	19.37	3.68	30.44

Fig. S4 SEM images of (a-b) Fe-NiSOH-10 min, (c-d) Fe-NiSOH-15 min, and (e-f) Fe-NiSOH-30 min with different magnifications. (g) Element amount of the Fe-NiSOH-x min (x = 10, 15, 20, and 30) electrodes obtained by EDX spectrum.

The influence of anodizing current densities for the Fe-NiSOH-x min electrodes can be qualitatively illustrated by their element amount. With the increase of anodizing times, the nanosheet structure of the catalysts remain well, while the atomic amount of S gradually decreases and Fe content increases. However, in the case of excessive anodizing time (such as 30 min), too many FeOOH nanosheets accumulate on the surface of the catalyst, which may impede mass transportation and result in poor catalytic activity (**Fig. S23**). Therefore, the optimal Fe-NiSOH catalyst is obtained at the current density of 8 mA cm^{-2} for 20 min.

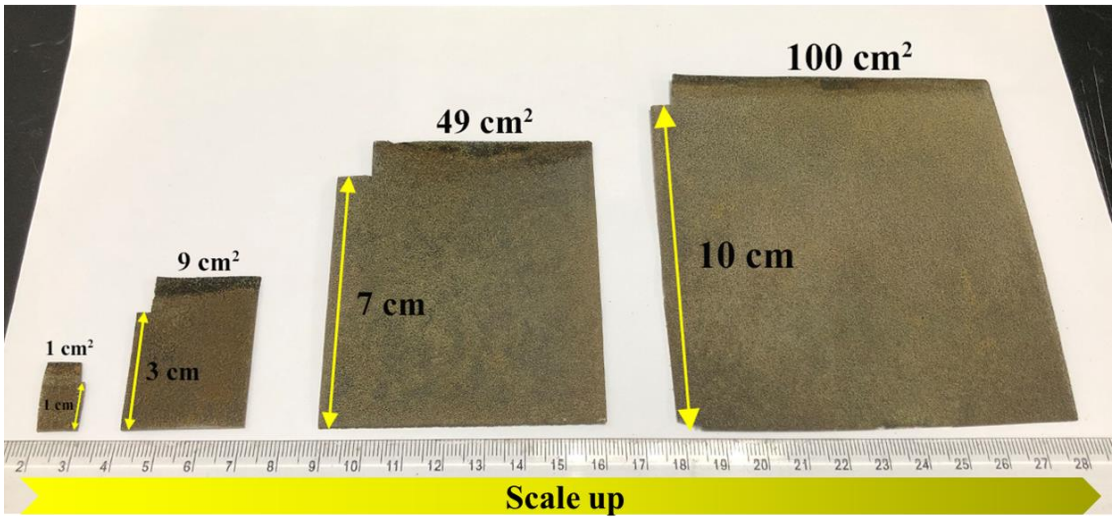

Fig. S5 Photograph of Fe-NiSOH catalysts *in-situ* grown on Ni foam at various scales (from 1 cm^2 to 100 cm^2).

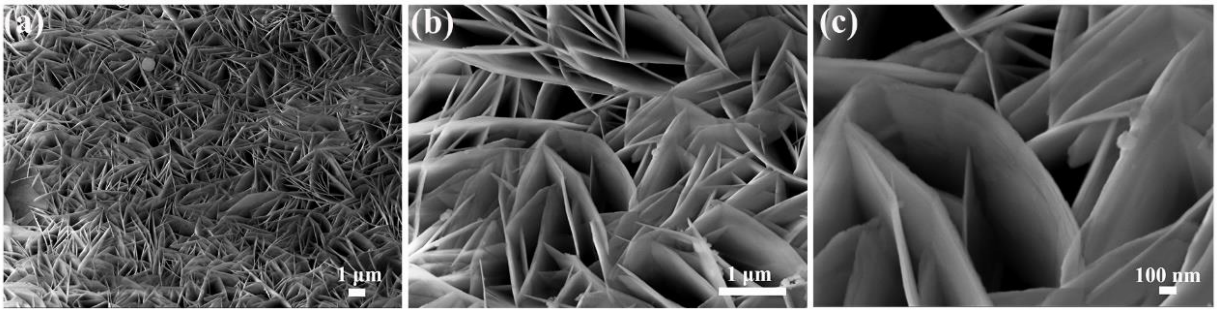

Fig. S6 SEM images of Ni-OH with different magnifications.

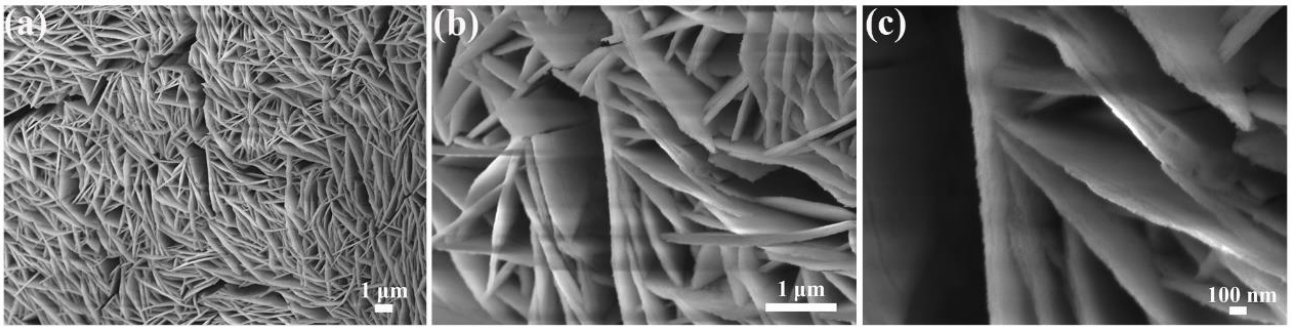

Fig. S7 SEM images of Fe-Ni-OH with different magnifications.

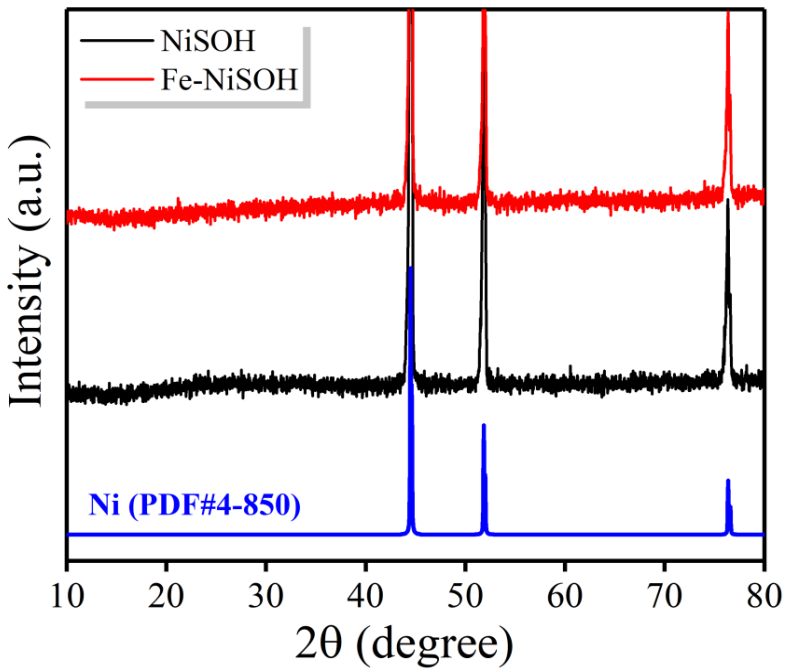

Fig. S8 XRD pattern of NiSOH and Fe-NiSOH.

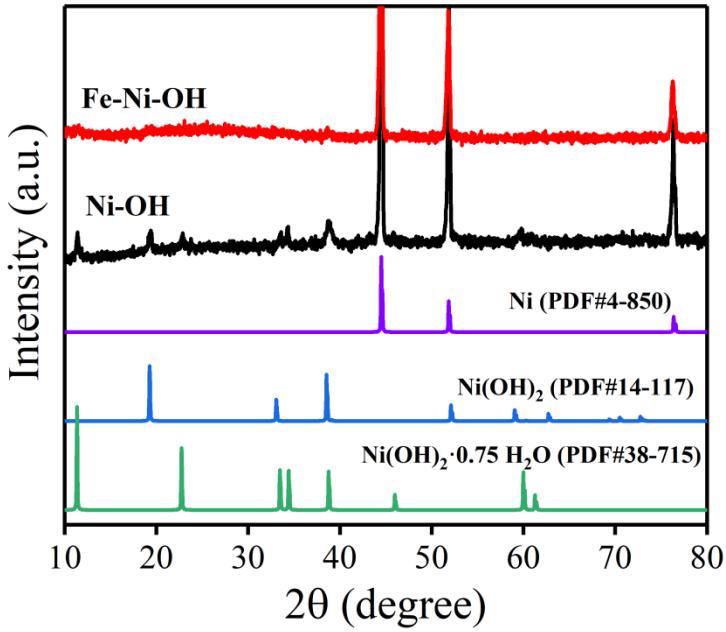

Fig. S9 XRD pattern of Ni-OH and Fe-Ni-OH.

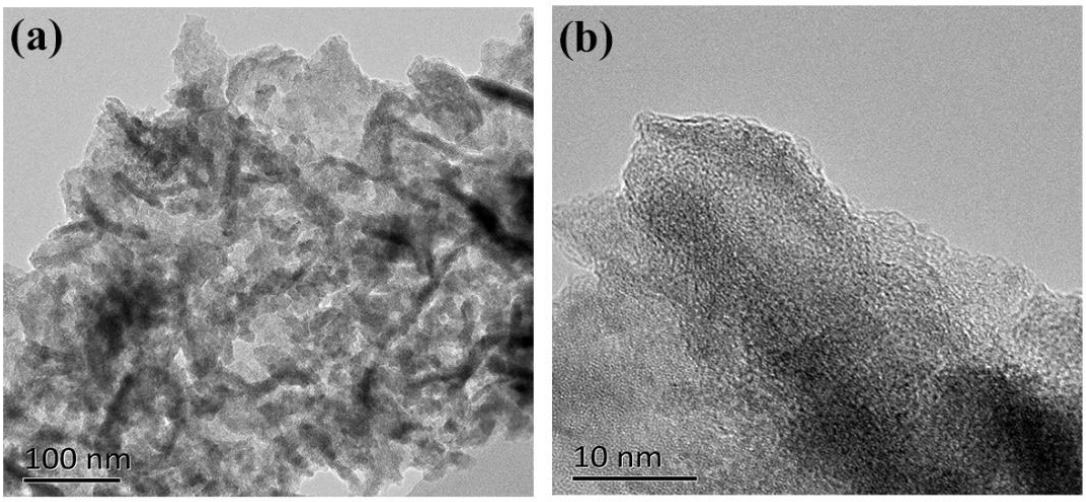

Fig. S10 TEM images of Fe-NiSOH with different magnifications.

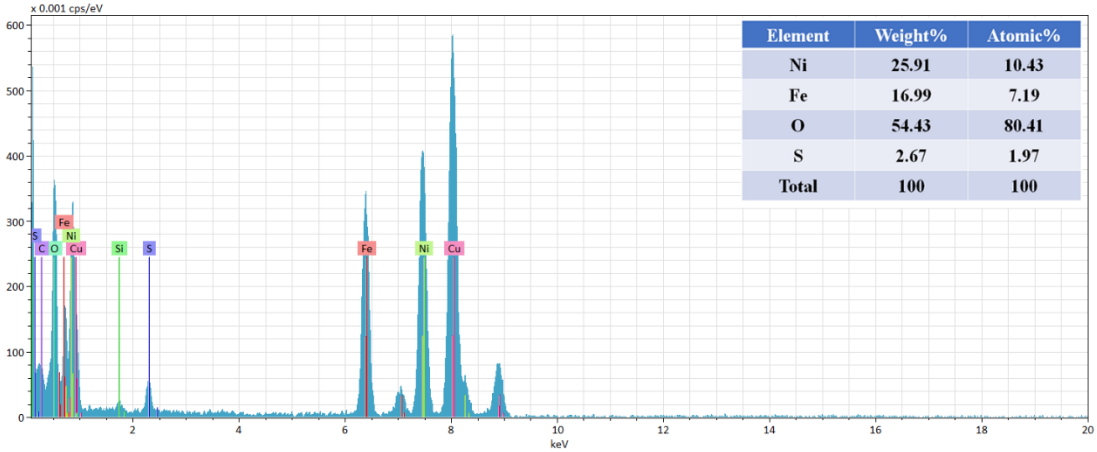

Element	Weight%	Atomic%
Ni	25.91	10.43
Fe	16.99	7.19
O	54.43	80.41
S	2.67	1.97
Total	100	100

Fig. S11 EDX spectrum of Fe-NiSOH.

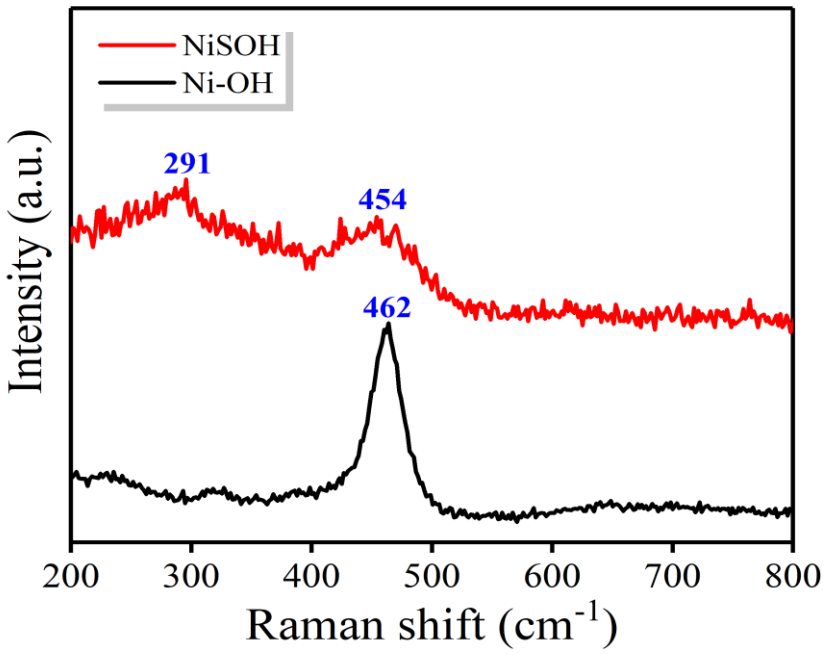

Fig. S12 Raman spectra of NiSOH and Ni-OH.

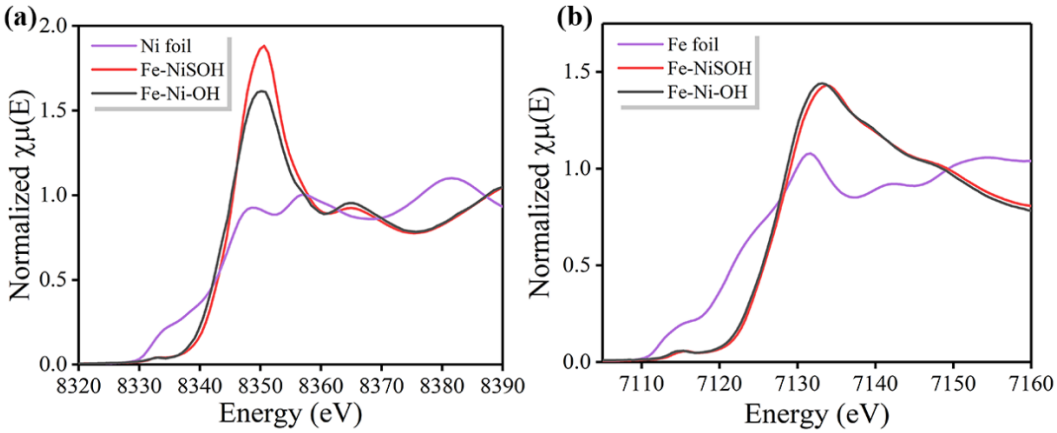

Fig. S13 Normalized (a) Ni and (b) Fe K-edge XANES spectra for Fe-NiSOH and Fe-Ni-OH.

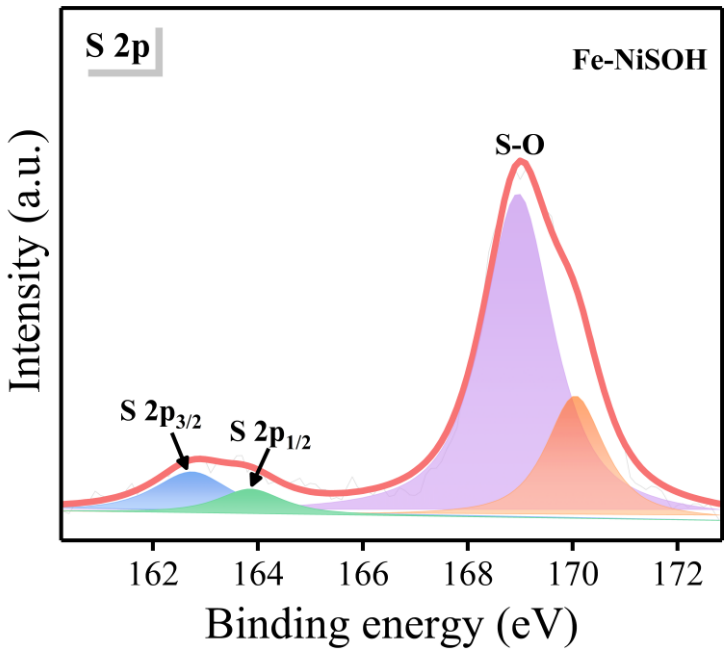

Fig. S14 High-resolution XPS spectrum of S 2p of Fe-NiSOH.

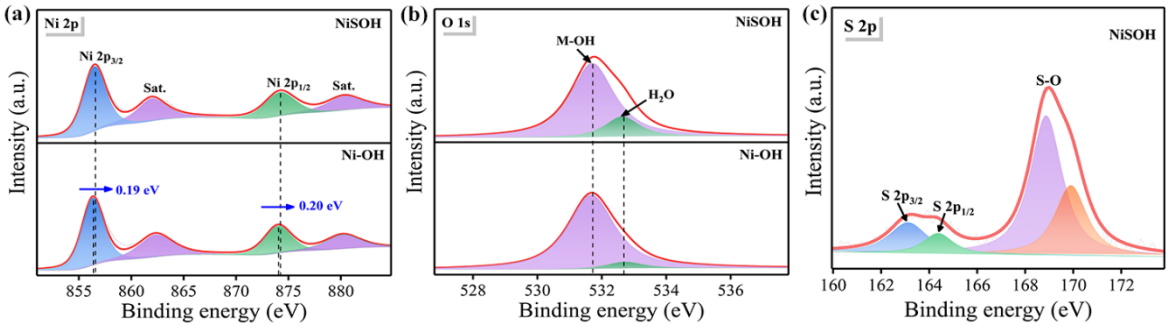

Fig. S15 High-resolution XPS spectra of (a) Ni 2p, (b) O 1s and (c) S 2p of Ni-OH and NiSOH.

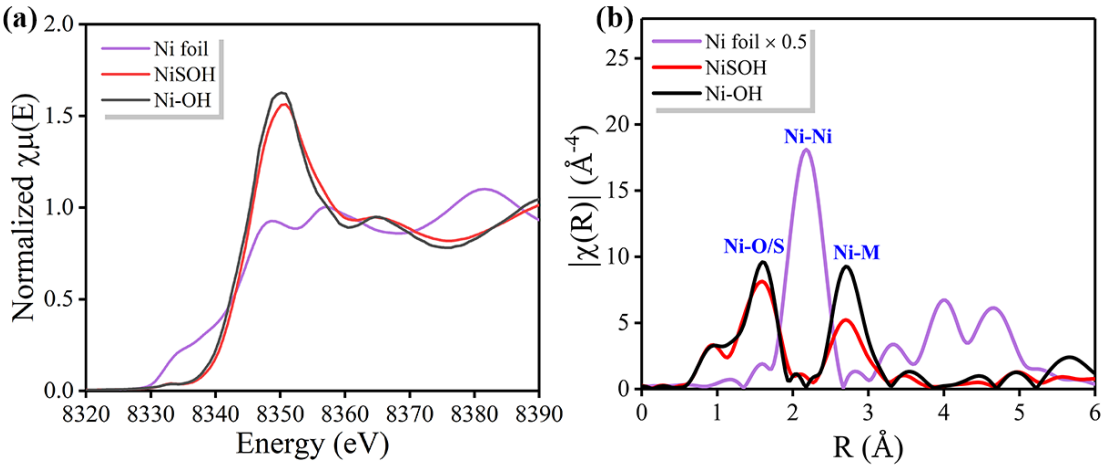

Fig. S16 (a) Normalized Ni K-edge XANES spectra for NiSOH and Ni-OH. (b) k^3-weighted FT-EXAFS spectra of Ni for NiSOH and Ni-OH, without phase shift correction.

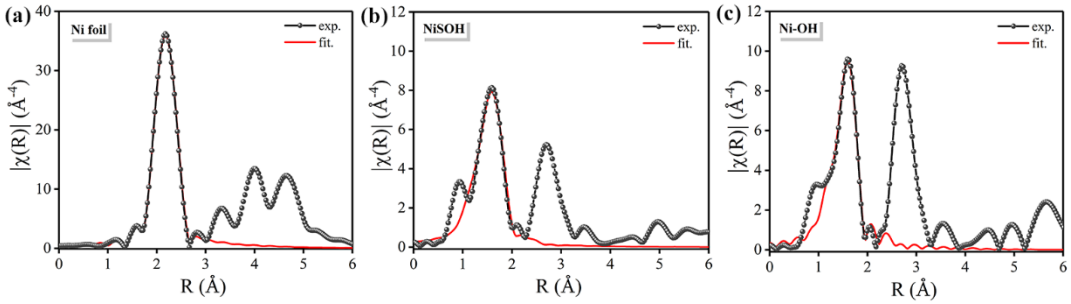

Fig. S17 EXAFS R-space fitting curves of Ni in (a) Ni foil, (b) NiSOH, and (c) Ni-OH.

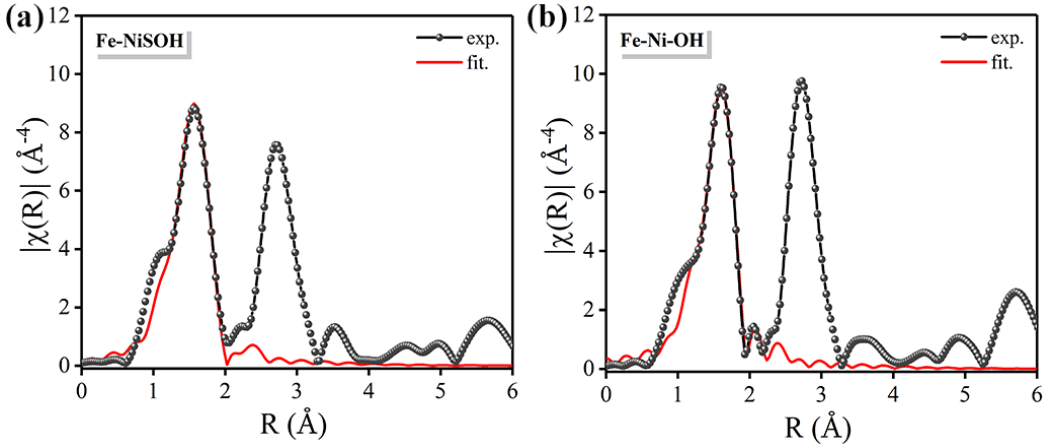

Fig. S18 EXAFS R-space fitting curves of Ni in (a) Fe-NiSOH and (b) Fe-Ni-OH.

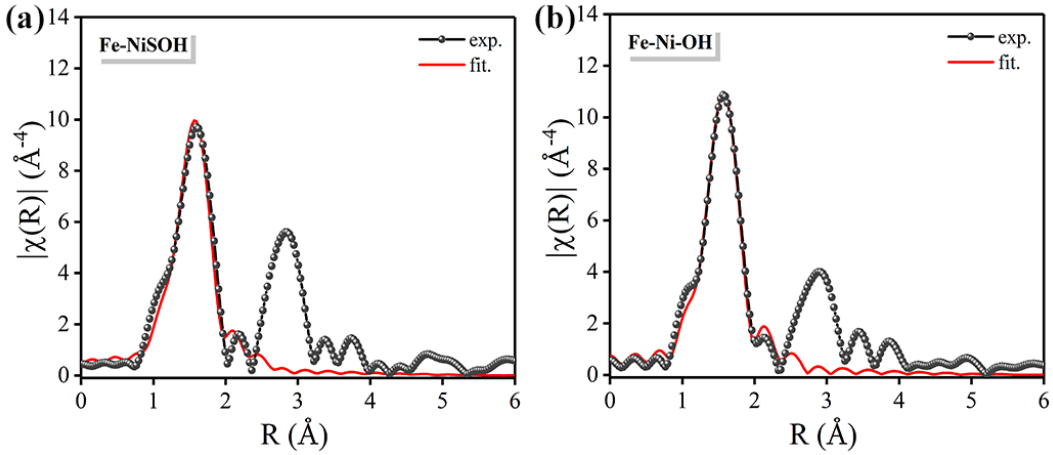

Fig. S19 EXAFS R-space fitting curves of Fe in (a) Fe-NiSOH and (b) Fe-Ni-OH.

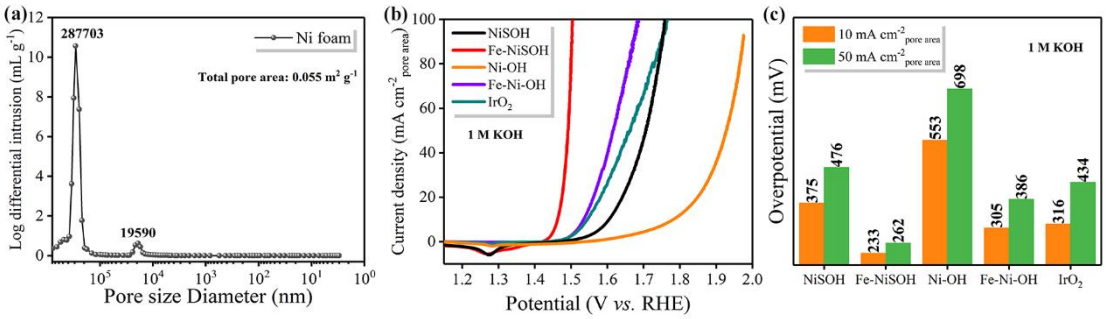

Fig. S20 (a) Pore size distribution of nickel foam substrate measured by mercury intrusion method. (b) Polarization curves of catalysts normalized by the total pore area of Ni foam. (c) Overpotentials of catalysts at different current densities.

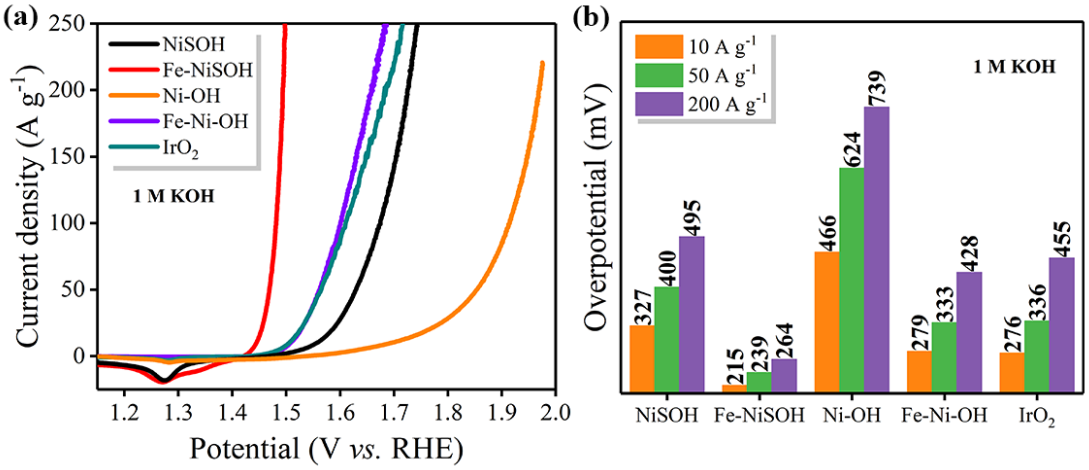

Fig. S21 (a) Polarization curves of catalysts normalized by loading mass. The loading amounts of NiSOH, Fe-NiSOH, Ni-OH, Fe-Ni-OH, and RuO_2 are about 2.158, 1.896, 2.792, 2.642, and 2.0 mg cm^{-2}, respectively. (b) Corresponding overpotentials at current densities of 10, 50, and 200 A g^{-1}.

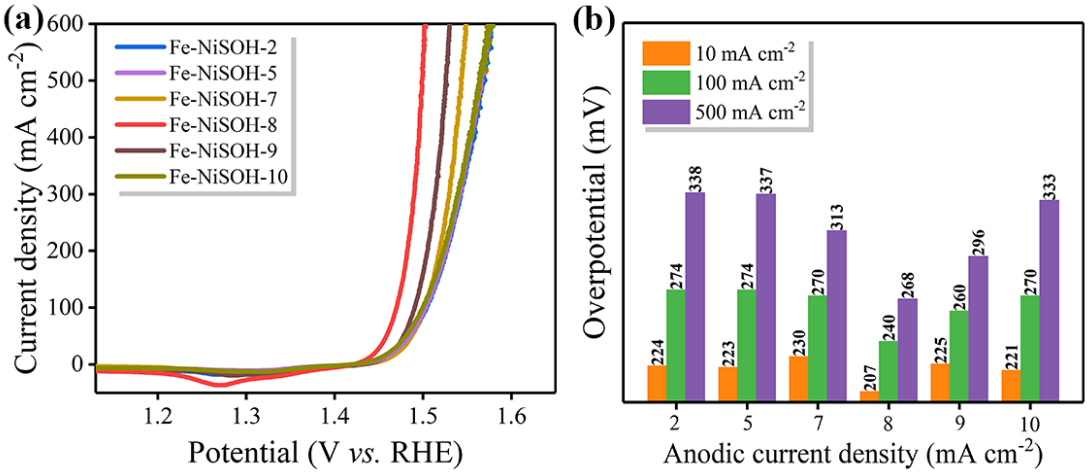

Fig. S22 (a) Polarization curves of Fe-NiSOH-x (x = 2, 5, 7, 8, 9, and 10) at a scan rate of 2 mV s^{-1} in 1 M KOH and (b) corresponding overpotentials at different current densities.

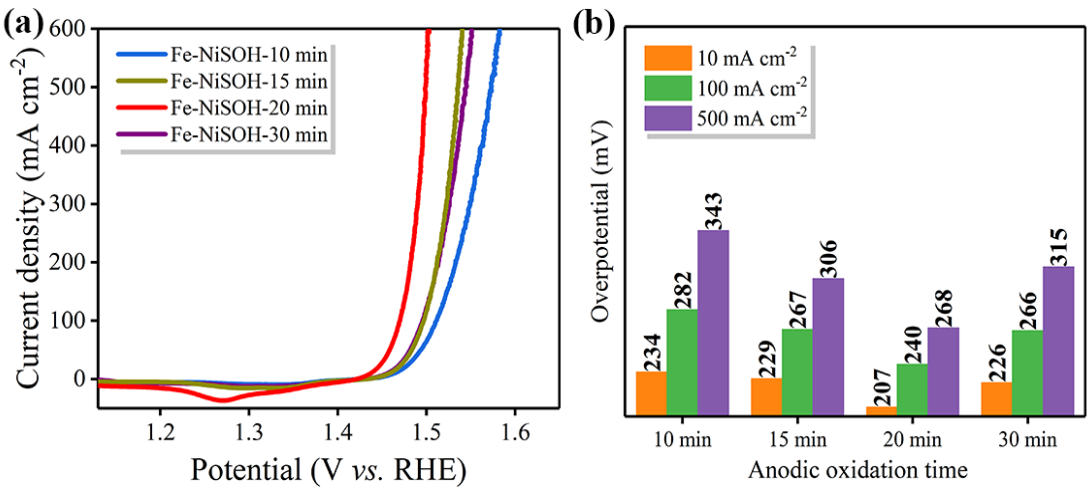

Fig. S23 (a) Polarization curves of Fe-NiSOH-x min (x = 10, 15, 20, and 30) at a scan rate of 2 mV s^{-1} in 1 M KOH and (b) corresponding overpotentials at different current densities.

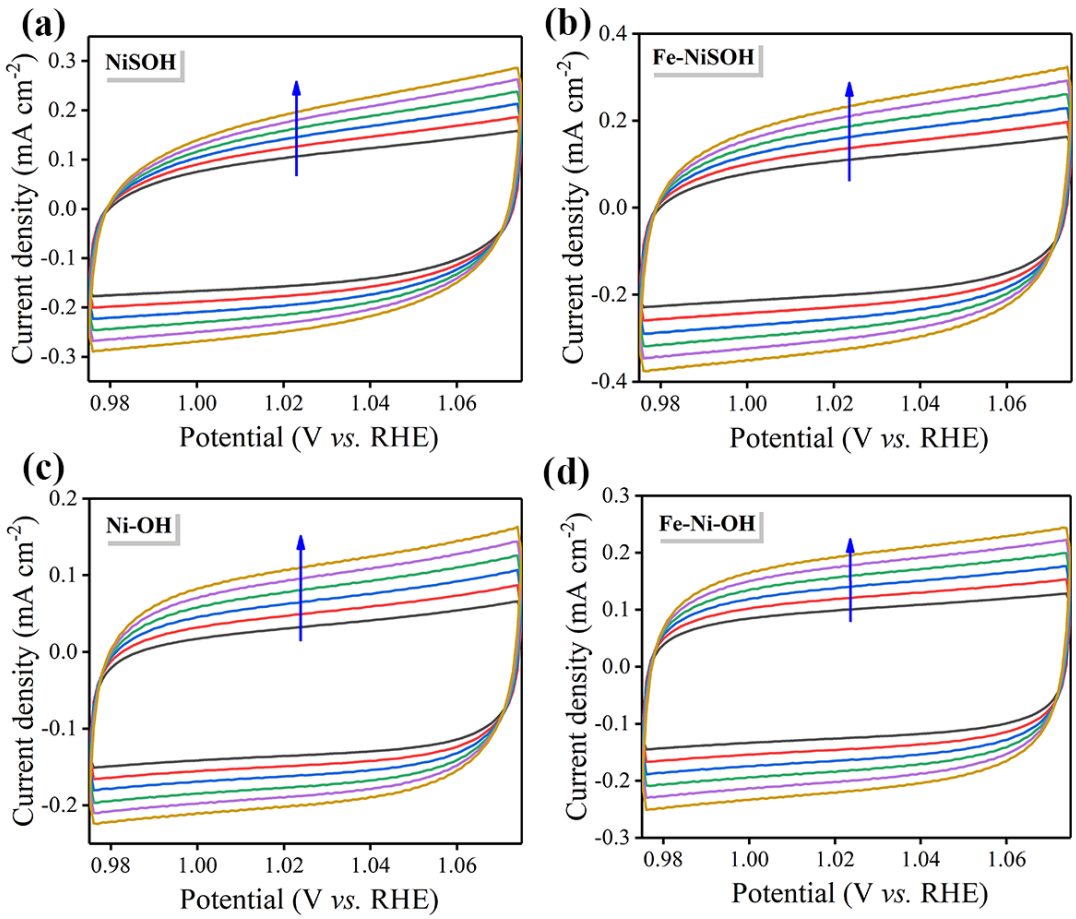

Fig. S24 CV curves of (a) NiSOH, (b) Fe-NiSOH, (c) Ni-OH, and (d) Fe-Ni-OH at scan rates of 50-100 mV s^{-1}.

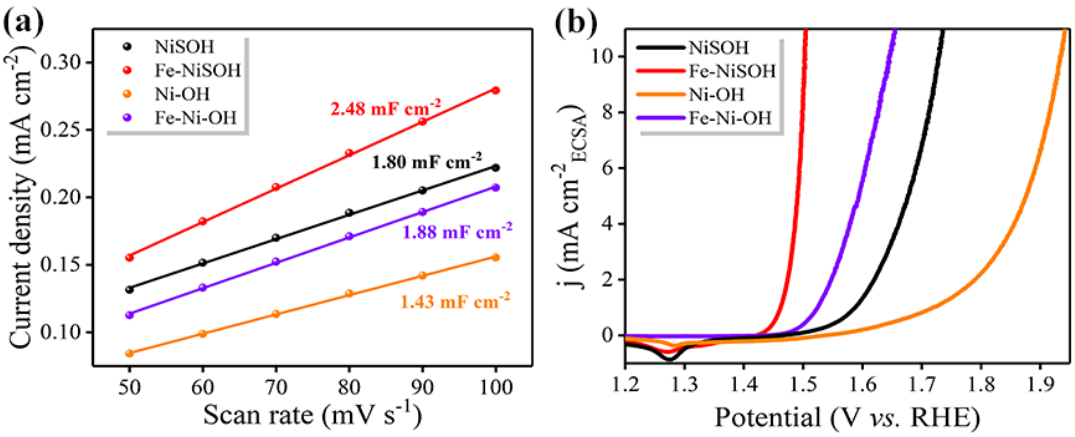

Fig. S25 (a) Double-layer capacitance (C_{dl}) plots, and (b) polarization curves normalized by ECSA of NiSOH, Fe-NiSOH, Ni-OH and Fe-Ni-OH electrodes.

The electrochemical active surface area (ECSA) of the catalysts was obtained by $ECSA = \frac{C_{dl}}{C_s}$, where specific capacitance C_s = 40 μF cm^{-2}.[5]

$ECSA_{NiSOH}$ = 1.80 mF cm^{-2}/40 μF cm^{-2} = 45.0 cm^{-2} $_{ECSA}$

$ECSA_{Fe\text{-}NiSOH}$ = 2.48 mF cm^{-2}/40 μF cm^{-2} = 62.0 cm^{-2} $_{ECSA}$

$ECSA_{Ni\text{-}OH}$ = 1.43 mF cm^{-2}/40 μF cm^{-2} = 35.8 cm^{-2} $_{ECSA}$

$ECSA_{Fe\text{-}Ni\text{-}OH}$ = 1.88 mF cm^{-2}/40 μF cm^{-2} = 47.0 cm^{-2} $_{ECSA}$

(a)

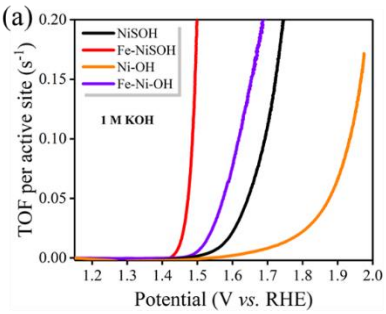

(b)

Catalysts	η = 250 mV	η = 350 mV
NiSOH	0.0005 s^{-1}	0.0138 s^{-1}
Fe-NiSOH	0.0635 s^{-1}	--
Ni-OH	--	0.0012 s^{-1}
Fe-Ni-OH	0.0020 s^{-1}	0.0558 s^{-1}

Fig. S26 (a) TOF curves and (b) The corresponding TOF values at overpotentials (η) of 250 and 350 mV for NiSOH, Fe-NiSOH, Ni-OH, and Fe-Ni-OH catalysts.

The turnover frequency (TOF) values of the catalysts were estimated from the equation:[6, 7] $TOF = \frac{j \cdot S}{4 \cdot F \cdot n}$, where j represents the OER current density (A cm^{-2}), S the real surface area of the working electrode, the number 4 a four-electron oxygen evolution reaction, F the Faraday's constant (96485.3 C mol^{-1}), and n the number of the moles of active atoms of catalysts, which can be calculated by the loading mass and the molecular weight of the catalysts.[8, 9] The total loading mass (2.792 mg cm^{-2} for Ni-OH, 2.642 mg cm^{-2} for Fe-Ni-OH, 2.158 mg cm^{-2} for NiSOH, and 1.896 mg cm^{-2} for Fe-NiSOH, respectively) were used by assuming that all the metal cations in the catalyst contribute to the catalytic current, and the calculated TOF values represent the lowest limit of TOF.[10]

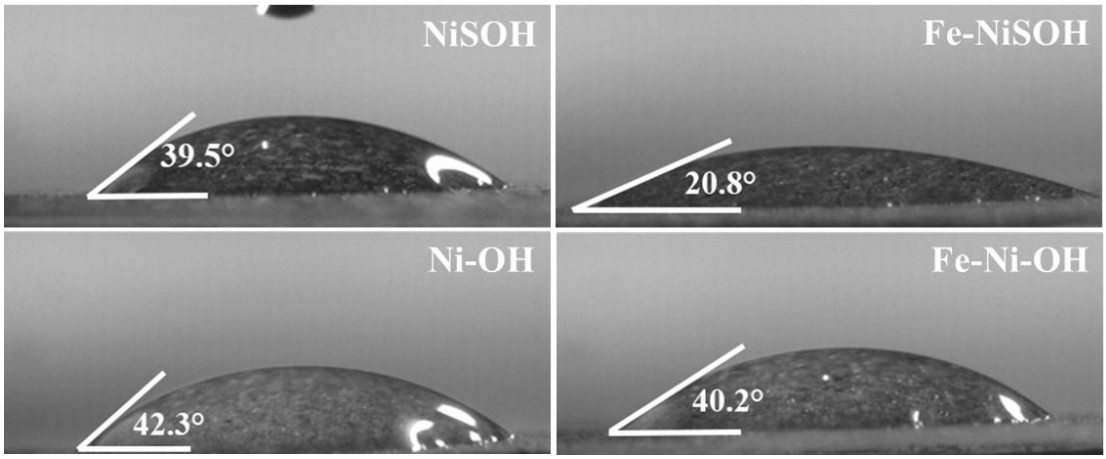

Fig. S27 Contact angle of NiSOH, Fe-NiSOH, Ni-OH, and Fe-Ni-OH. (In order to avoid the influence of the pore structure of nickel foam substrate on contact angle measurement, the nickel foam loaded with catalyst was pressed into a film by a tablet press before measurement.)

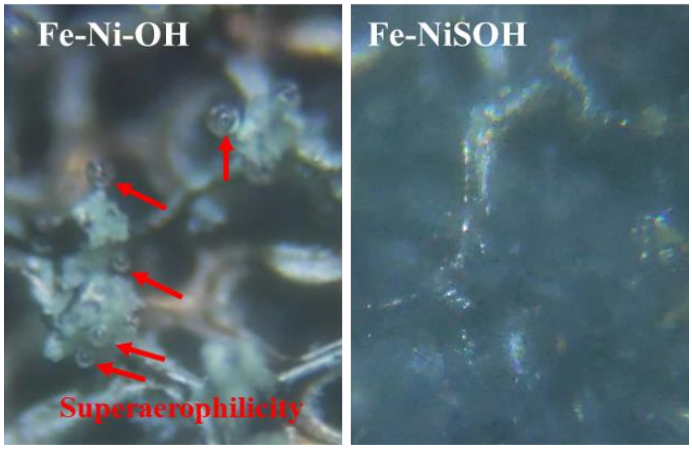

Fig. S28 Photograph of bubble releasing behaviors for the Fe-Ni-OH and Fe-NiSOH electrodes at a constant current density of 10 mA cm^{-2}. (The corresponding dynamic process is shown in the **Video S1** for Fe-Ni-OH and **Video S2** for Fe-NiSOH, respectively.)

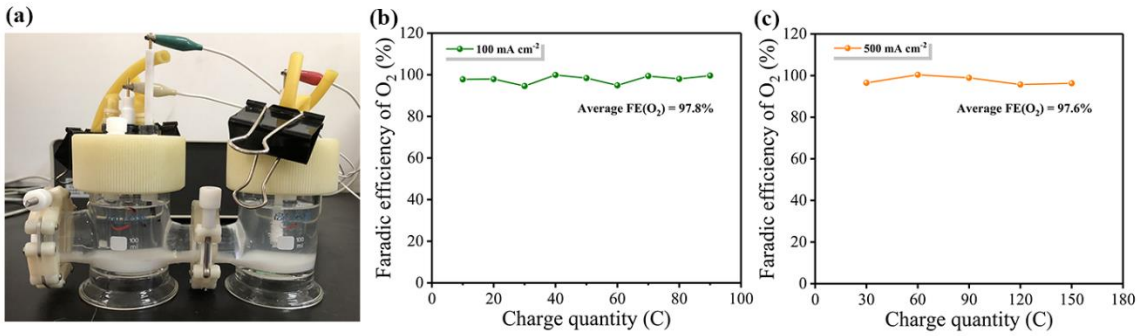

Fig. S29 (a) Digital photographs of H-type electrolytic cell with 1 M KOH seawater. (b) Faradic efficiency of O_2 for Fe-NiSOH detected in 1 M KOH seawater under current densities of (a) 100 and (b) 500 mA cm^{-2}.

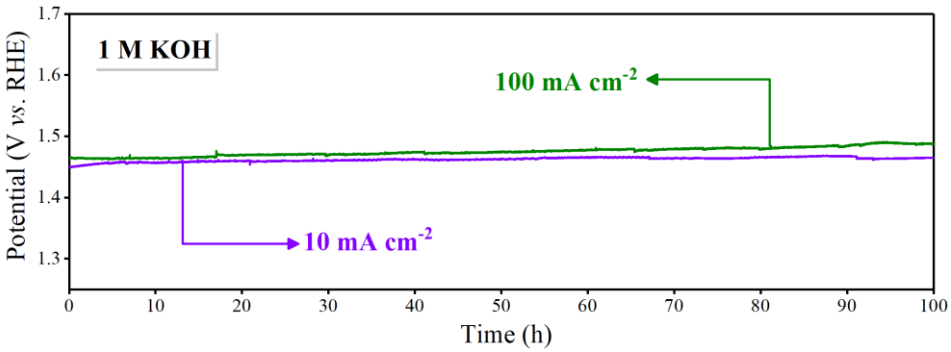

Fig. S30 Chronopotentiometry curves of Fe-NiSOH at current densities of 10 and 100 mA cm^{-2} in 1 M KOH.

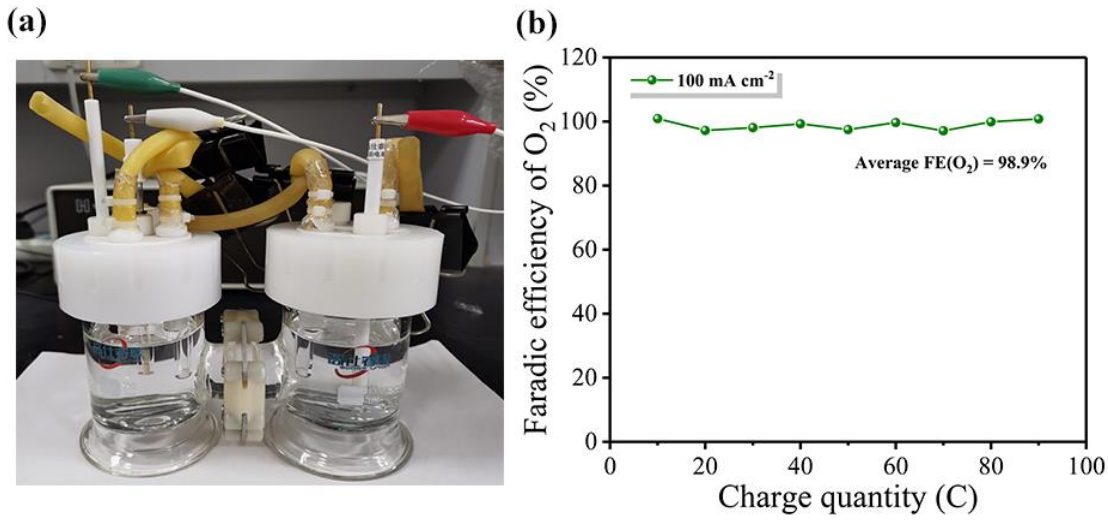

Fig. S31 (a) Digital photographs of H-type electrolytic cell with 1 M KOH. (b) Faradic efficiency of O_2 for Fe-NiSOH detected in 1 M KOH under a current density of 100 mA cm^{-2}.

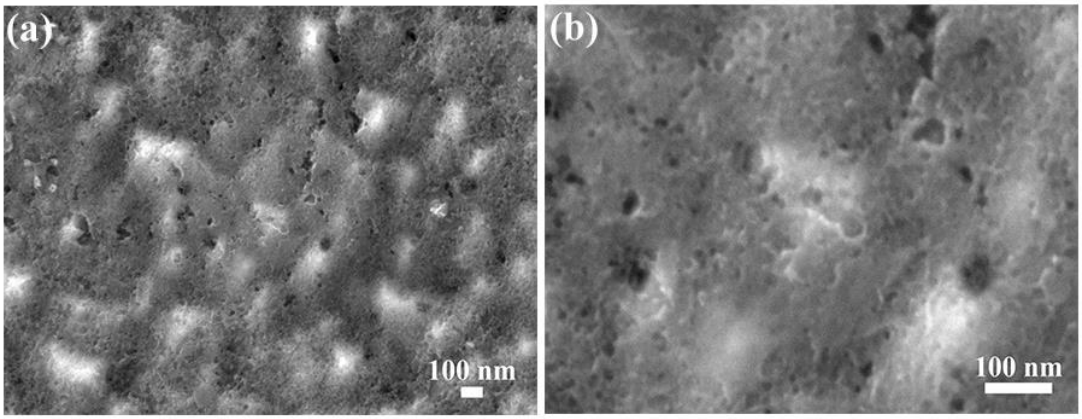

Fig. S32 SEM image of Fe-NiSOH after 100-h OER test at current density of 10 mA cm^{-2} in 1 M KOH.

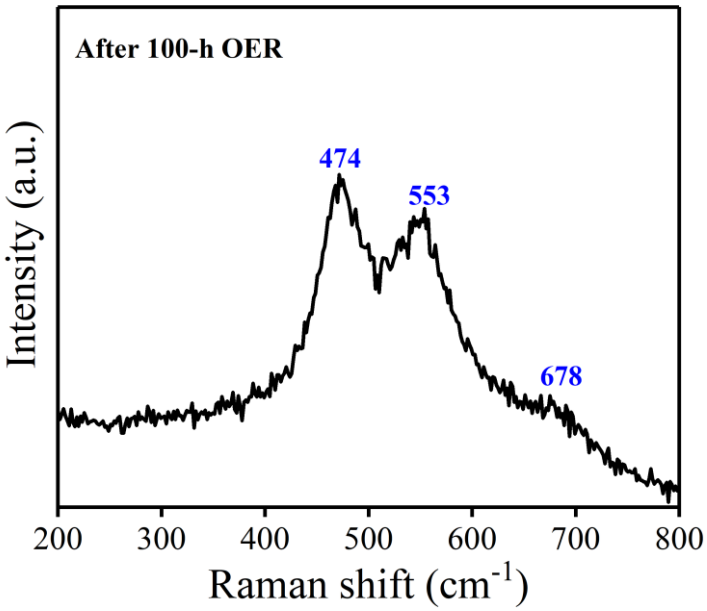

Fig. S33 Raman spectrum of Fe-NiSOH after 100-h OER test at current density of 10 mA cm^{-2} in 1 M KOH.

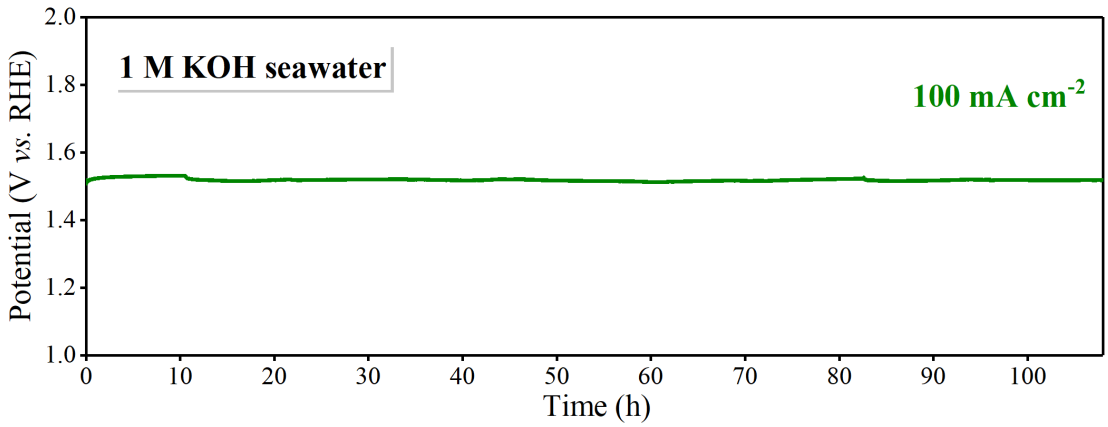

Fig. S34 Chronopotentiometry curves of Fe-NiSOH at current densities of 100 mA cm^{-2} in 1 M KOH seawater.

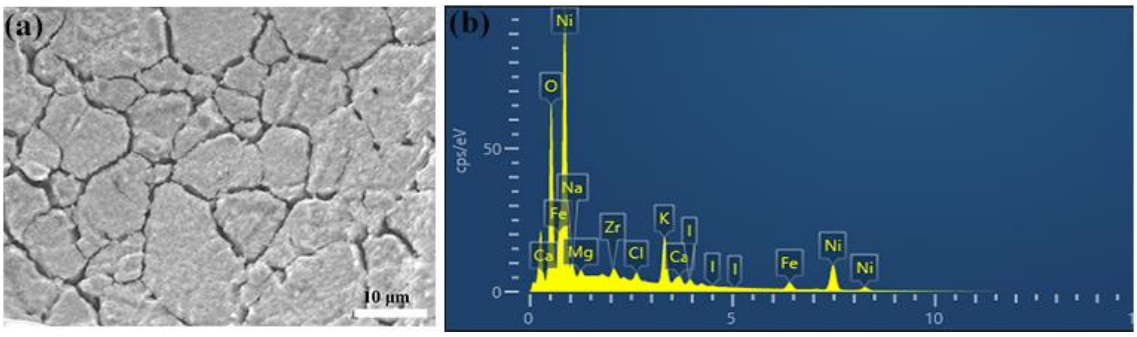

Fig. S35 (a) SEM image and (b) EDX spectrum of the Fe-NiSOH electrode after 100-h OER operation under 100 mA cm^{-2} in 1 M KOH seawater.

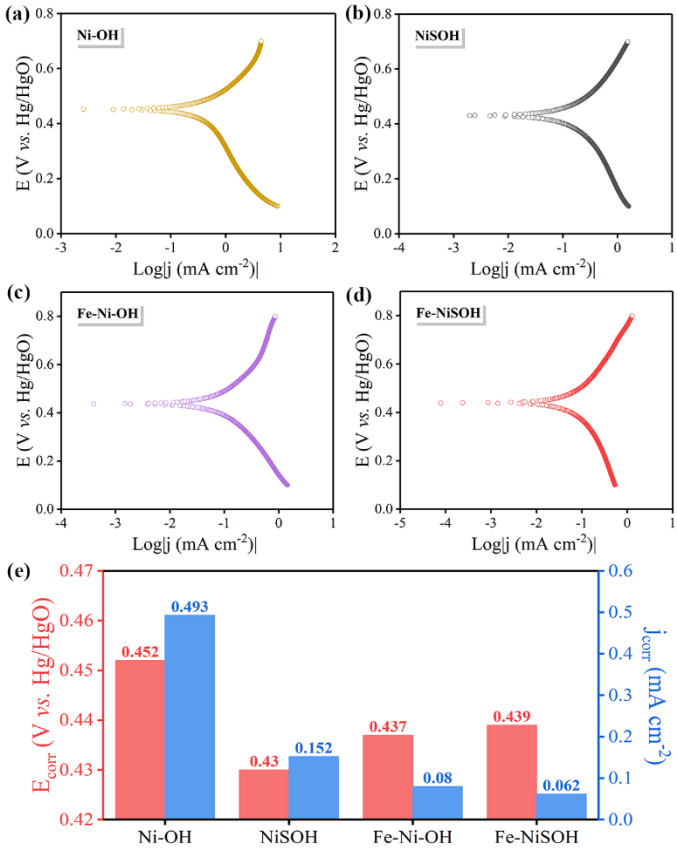

Fig. S36 Corrosion polarization curves of (a) Ni-OH, (b) NiSOH, (c) Fe-Ni-OH, and (d) Fe-NiSOH tested in the natural seawater. (e) Corrosion potential (E_{corr}) and corrosion current density (j_{corr}) of the catalysts in natural seawater.

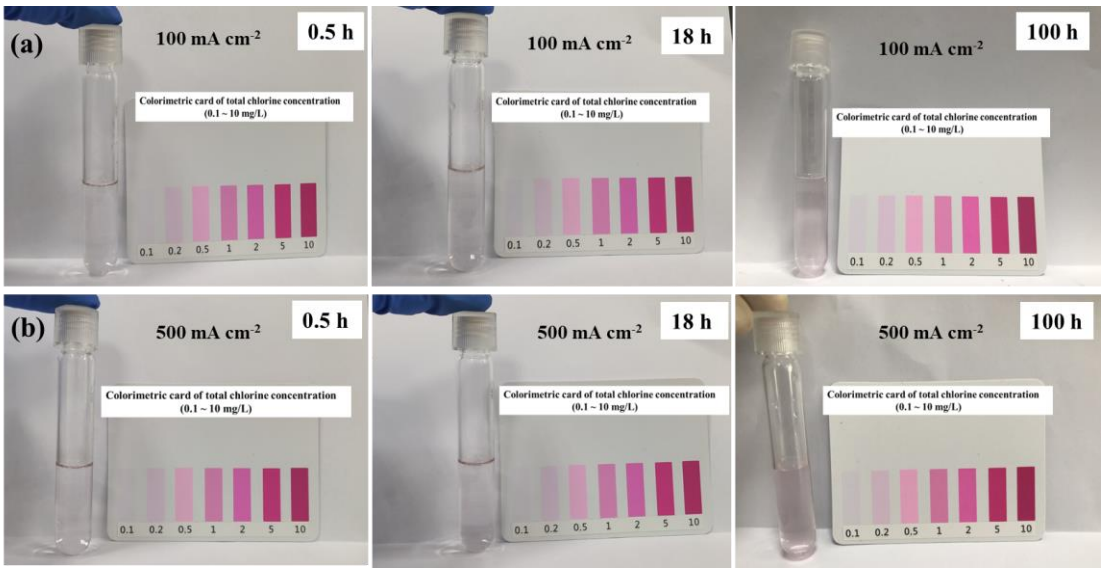

Fig. S37 Testing results for ClO^- formation in 1 M KOH seawater electrolytes during 100-h seawater splitting under current densities of (a) 100 and (b) 500 mA cm^{-2}.

The ClO^- generated in the electrolytes was detected by a colorimetric method. Firstly, the pH value of the electrolytes was adjusted to 7-8 by acetic acid, and then 5 ml of the above solution was put into a colorimetric tube. A small package of N, N-diethyl-pphenylenediamine (DPD) reagent was subsequently added to the colorimetric tube, which was shaken for DPD dissolution. After standing for 3 minutes, the concentration of ClO^- in the electrolytes was detected by comparing the color of the solution with the color cards. As shown in the above figures, only a very small amount of ClO^- is formed in the electrolytes after 100-h seawater splitting under current densities of 100 ($c < 0.1$ mg L^{-1}) and 500 mA cm^{-2} (0.1 mg $L^{-1} < c < 0.2$ mg L^{-1}), indicating its excellent OER selectivity.

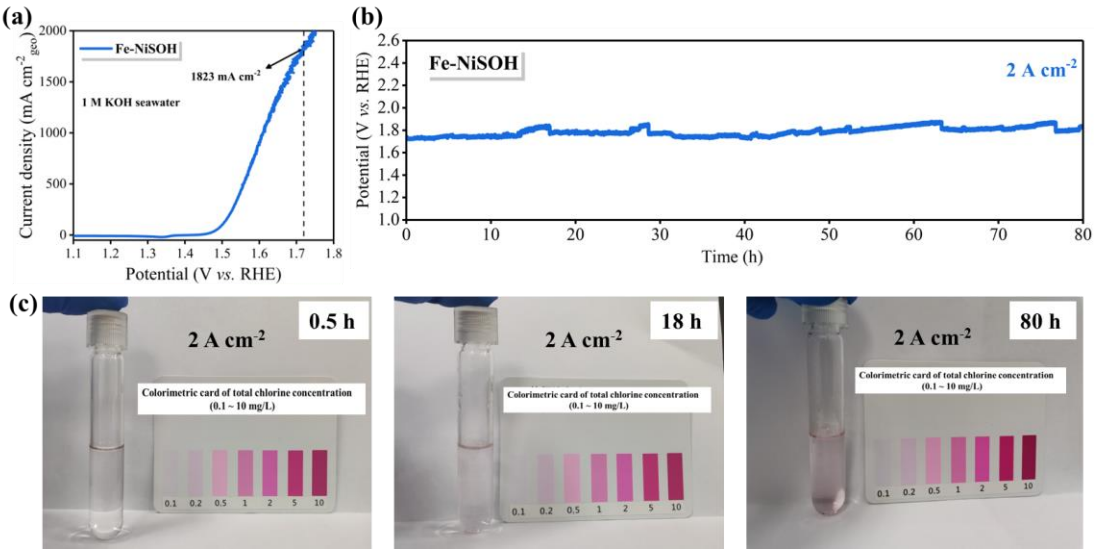

Fig. S38 (a) OER polarization curve of Fe-NiSOH at a scan rate of 2 mV s^{-1} in 1 M KOH seawater with potential over 1.72 V *vs.* RHE. (b) Chronopotentiometry curve of Fe-NiSOH at current density of 2 A cm^{-2} in 1 M KOH seawater. (c) Testing results for ClO^- formation in 1 M KOH seawater electrolyte during 80-h seawater splitting under large current density of 2 A cm^{-2}. (Only small amount of ClO^- is formed in the electrolyte during 80-h seawater splitting under large current density of 2 A cm^{-2}, suggesting its excellent OER selectivity.)

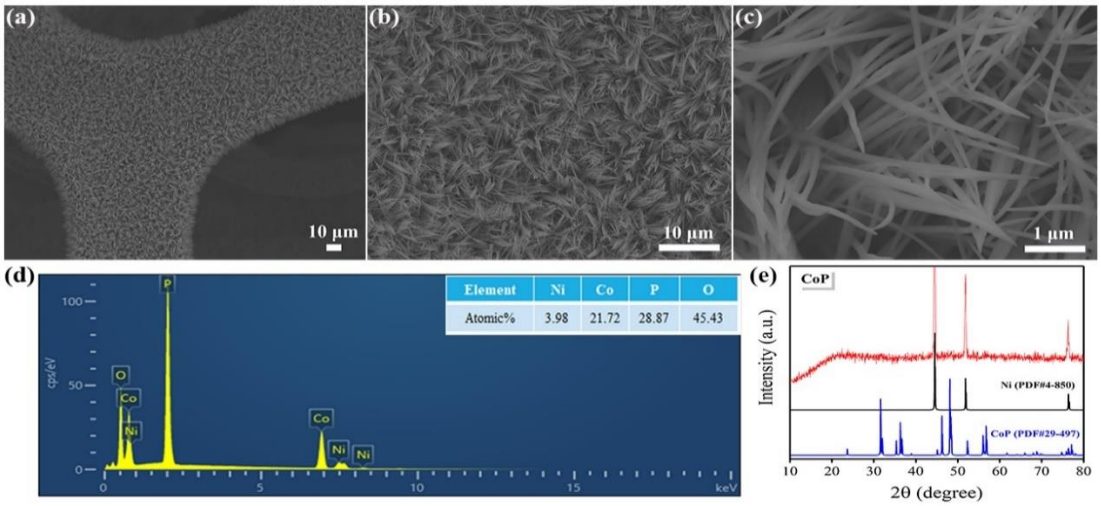

Fig. S39 (a-c) SEM images, (d) EDX spectrum, and (e) XRD pattern of CoP nanorod arrays on Ni foam.

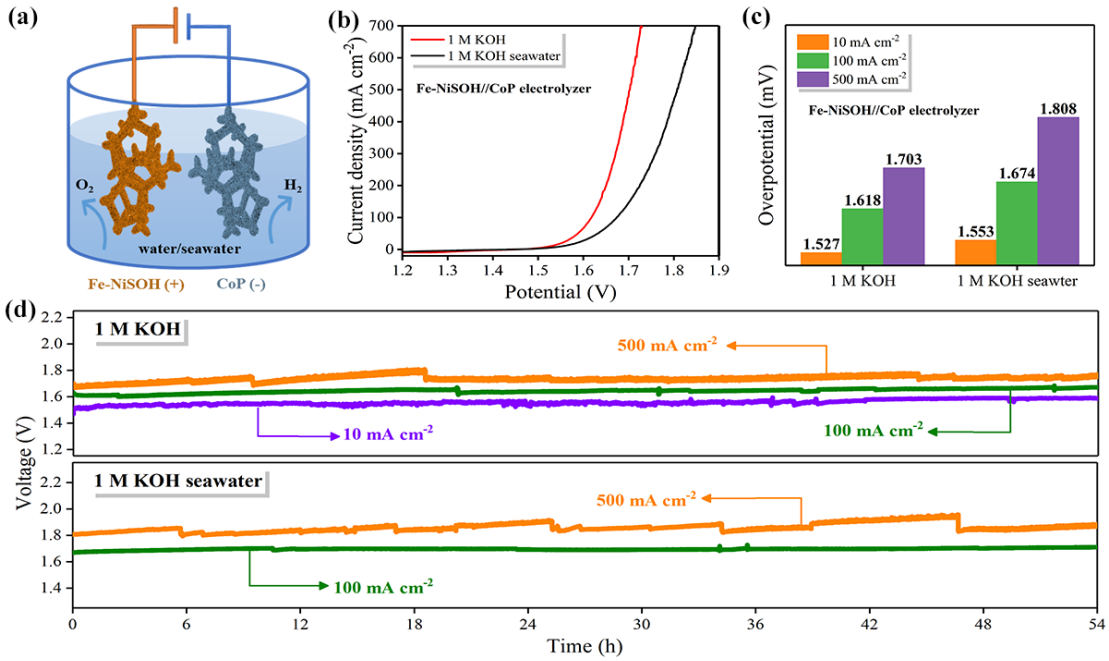

Fig. S40 (a) Schematic illustration of Fe-NiSOH//CoP electrolyzer. (b) LSV curves of Fe-NiSOH//CoP electrolyzer in alkaline water/seawater. (c) Overpotential of current densities of 10, 100, and 500 mA cm^{-2} for the electrolyzer in 1 M KOH and 1 M KOH seawater. (d) Chronopotentiometry curves of the Fe-NiSOH//CoP electrolyzer at different current densities in 1 M KOH and 1 M KOH seawater.

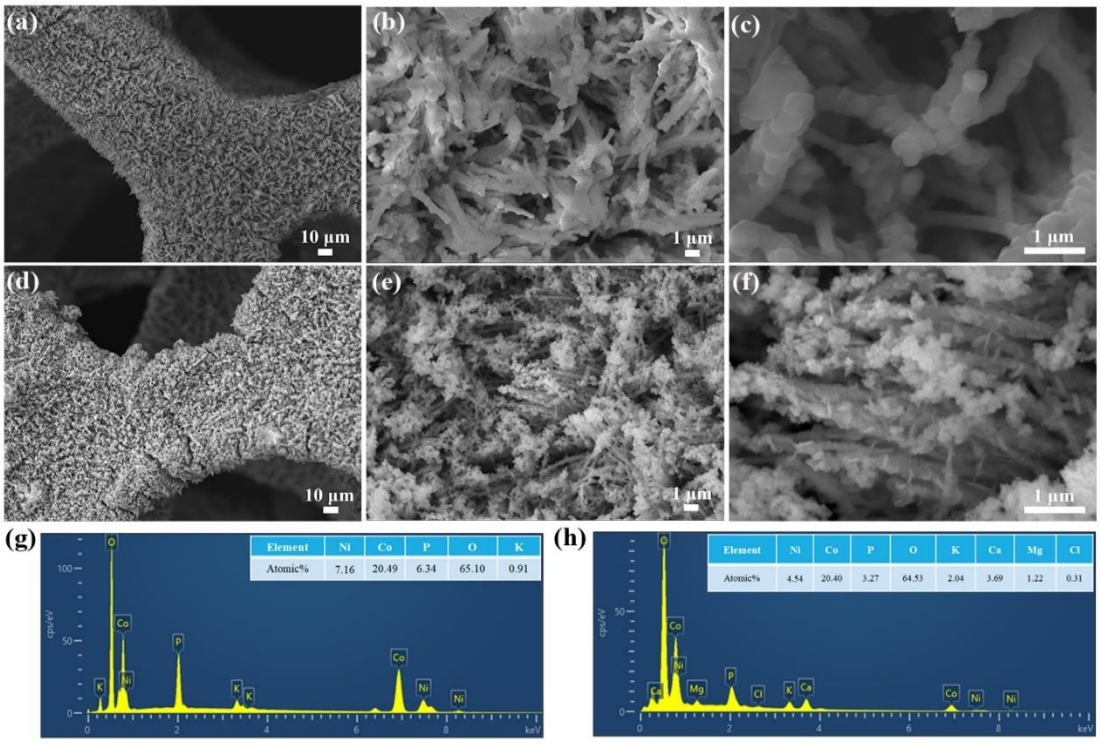

Fig. S41 SEM images of CoP nanorod arrays on Ni foam after 54-hour overall water splitting in (a-c) 1 M KOH and (d-f) 1 M KOH seawater at constant current density of 500 mA cm^{-2}. EDX spectrum of CoP electrodes after 54-hour overall water splitting in (g) 1 M KOH and (h) 1 M KOH seawater.

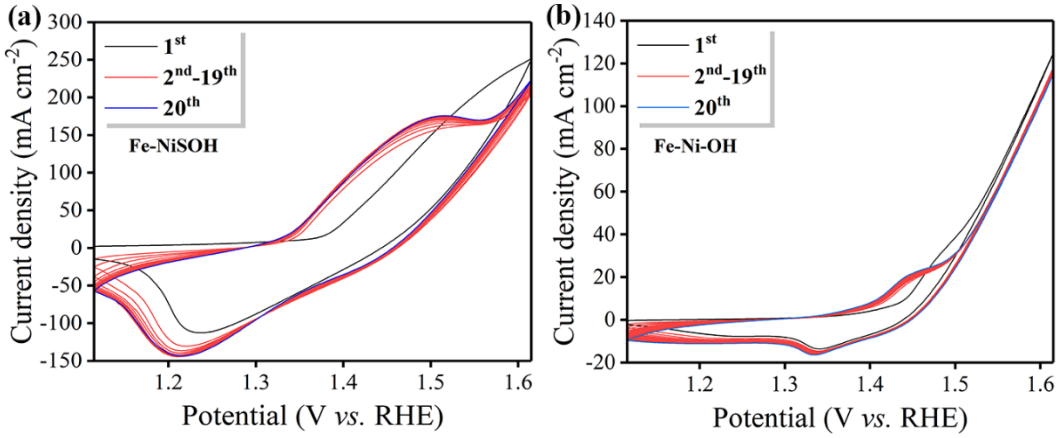

Fig. S42 CV curves of Fe-NiSOH and Fe-Ni-OH without IR correction. As the CV measurement progressed, both catalysts showed increasing redox current densities and remained stable at the 20th cycle, indicating that they reached the steady state.

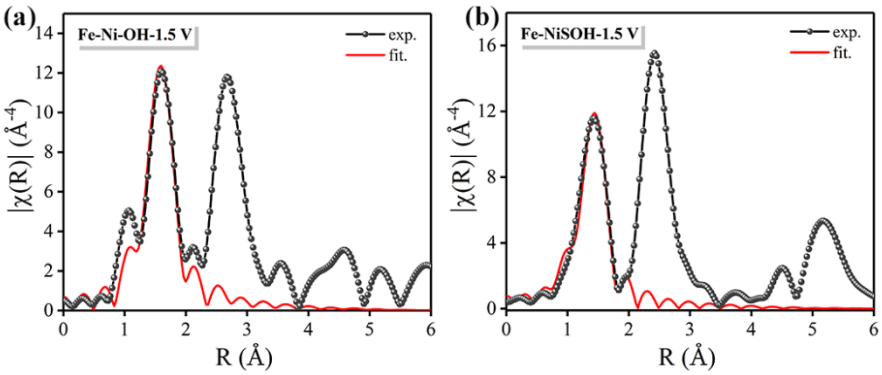

Fig. S43 EXAFS R-space fitting curves of Ni in (a) Fe-Ni-OH and (b) Fe-NiSOH at 1.5 V *vs*. RHE.

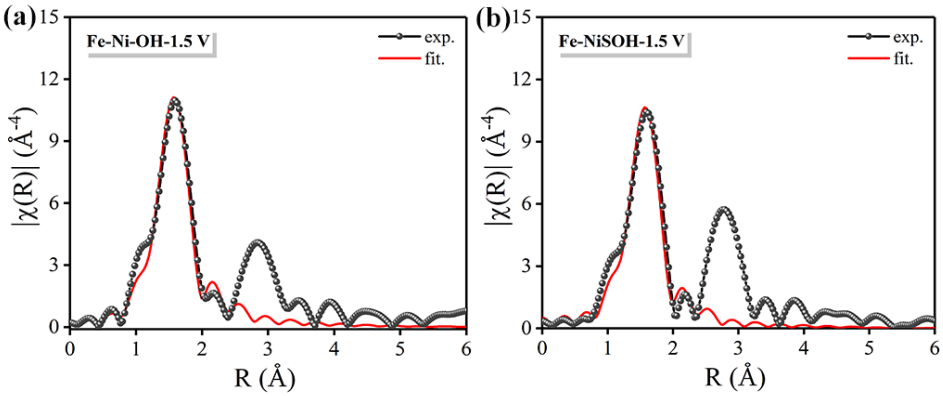

Fig. S44 EXAFS R-space fitting curves of Fe in (a) Fe-Ni-OH and (b) Fe-NiSOH at 1.5 V *vs*. RHE.

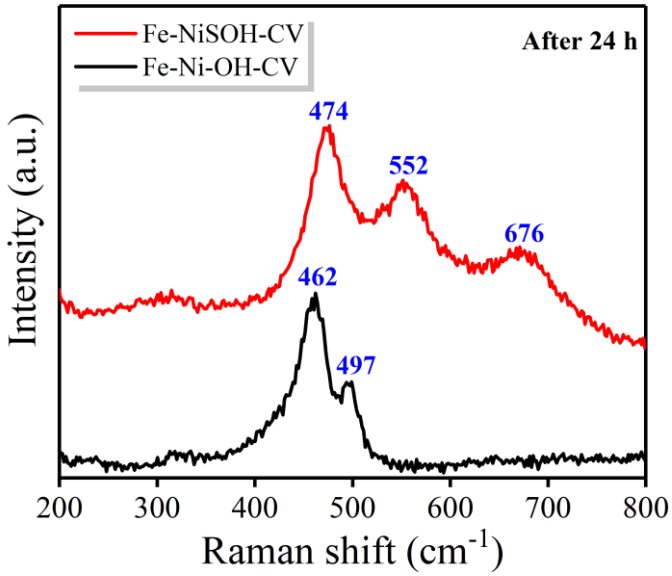

Fig. S45 Raman spectrum of Fe-NiSOH-CV and Fe-Ni-OH-CV after 24 h exposure to air.

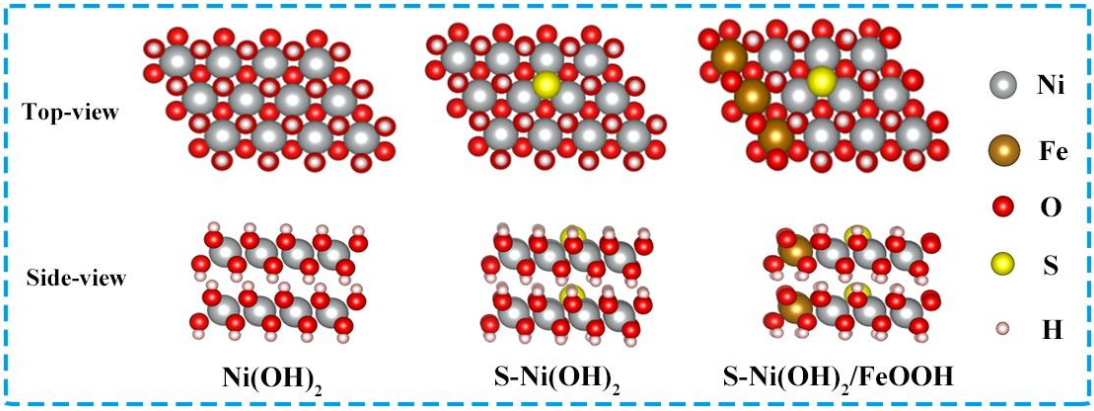

Fig. S46 Top-view and side-view of the optimited models of $Ni(OH)_2$, S-$Ni(OH)_2$, and S-$Ni(OH)_2$/FeOOH.

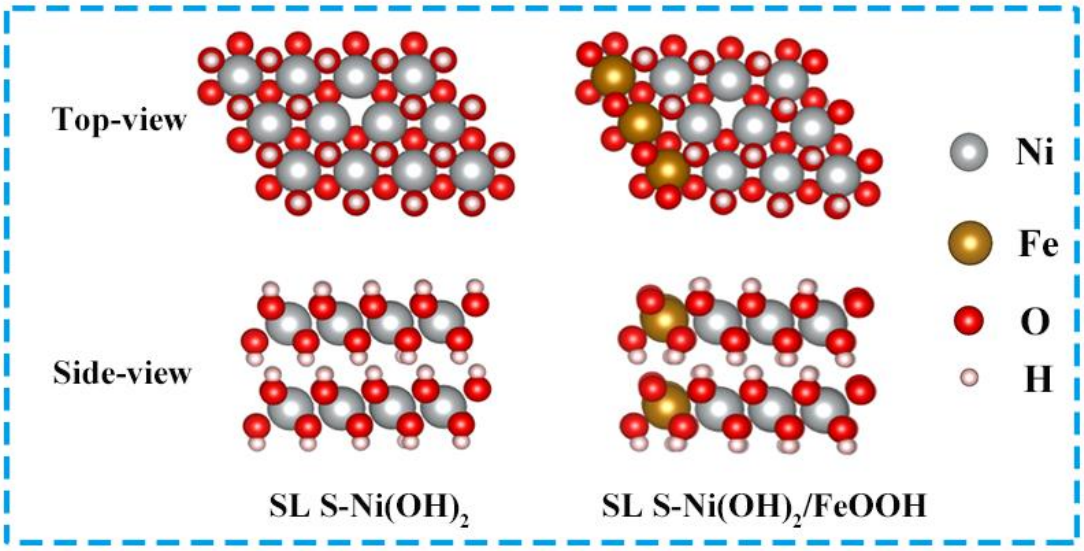

Fig. S47 Top-view and side-view of the optimited models of SL S-$Ni(OH)_2$, and SL S-$Ni(OH)_2$/FeOOH.

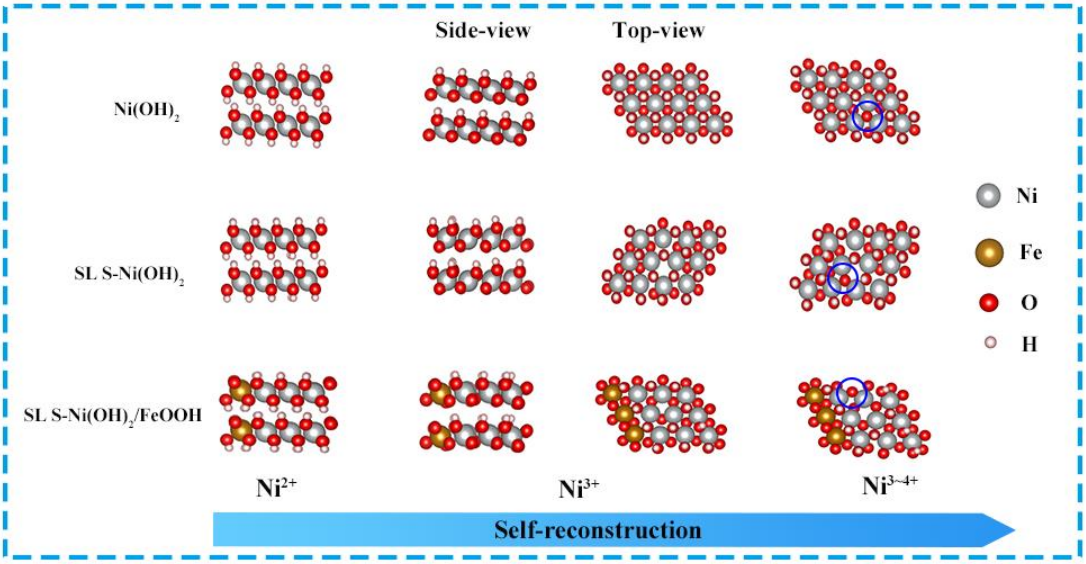

Fig. S48 Optimited models structures of $Ni(OH)_2$, SL S-$Ni(OH)_2$, and SL S-$Ni(OH)_2$/FeOOH during self-reconstruction.

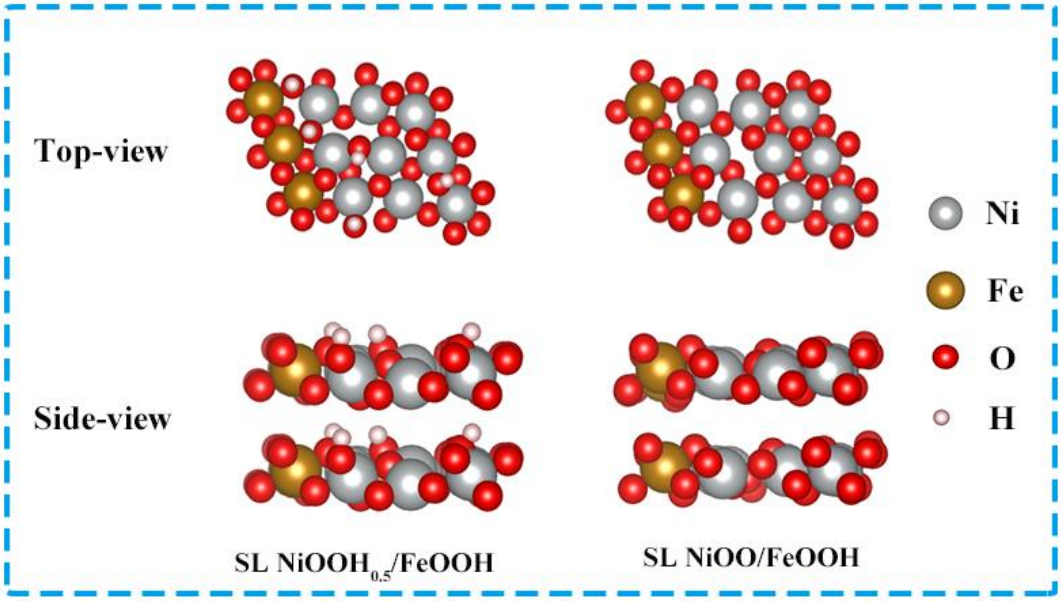

Fig. S49 Top-view and side-view of the optimited models of SL $NiOOH_{0.5}$/FeOOH and SL NiOO/FeOOH.

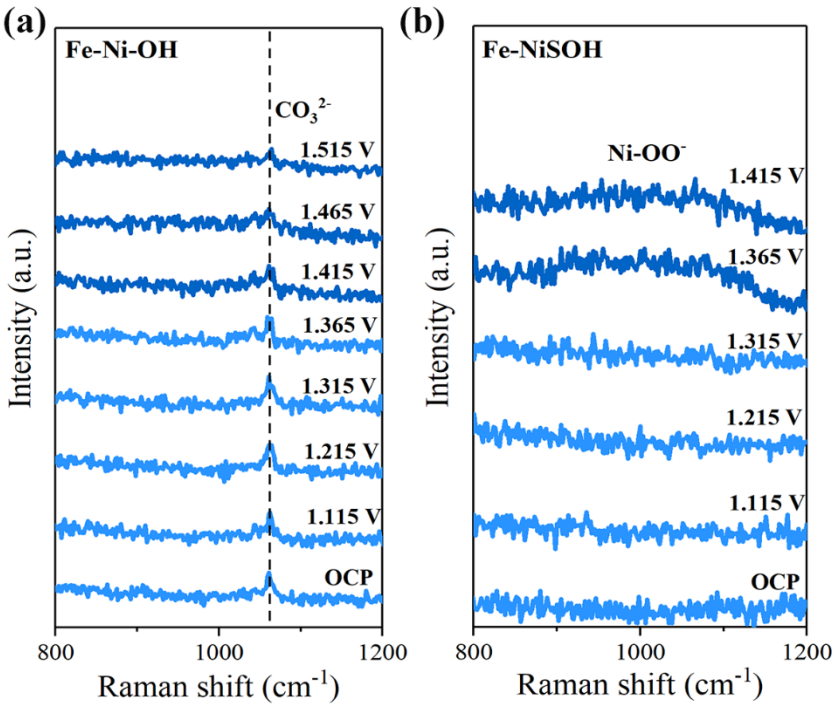

Fig. S50 *In situ* Raman spectrum of (a) Fe-Ni-OH and (b) Fe-NiSOH at the range from 800 ~ 1200 cm^{-1}.

When being operated at OCP, the peak at about 1062 cm^{-1} of the Fe-Ni-OH corresponds to residual CO_3^{2-} from the decomposition of the urea during sample preparation.[11, 12] No active oxygen species appear on the Raman spectrum, even though the applied potential is increasing. As for the Fe-NiSOH, there is a broad peak between 850-1150 cm^{-1} when being operated at 1.365 V *vs*. RHE, ascribed to Ni-OO$^-$.[13, 14]

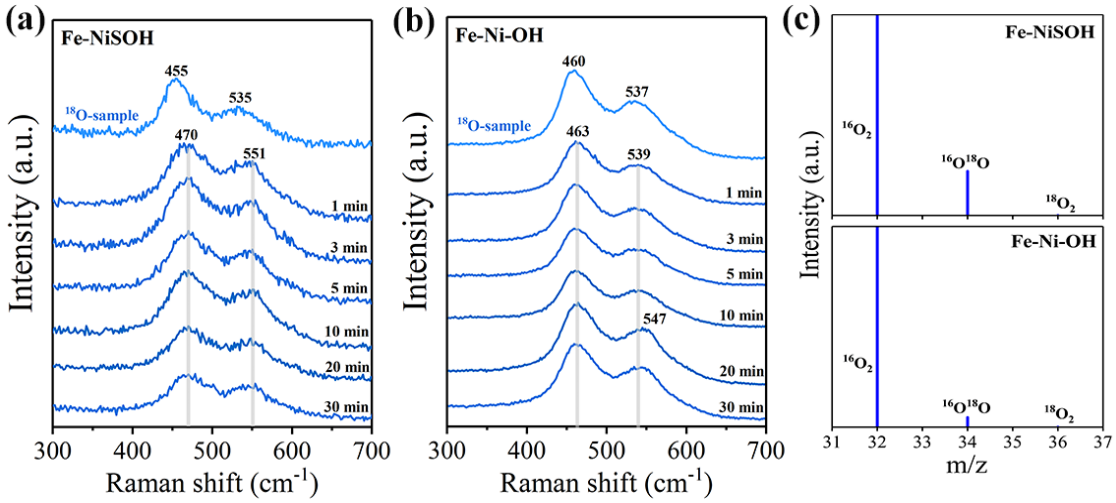

Fig. S51 *In-situ* Raman spectra of ^{18}O-labelled (a) Fe-NiSOH and (b) Fe-Ni-OH measured at a constant current density of 10 mA cm^{-2} in 1 M KOH with $H_2{}^{16}O$ for different time (1 min to 30 min). (c) Detected MS signals of generated oxygen product using ^{18}O isotope-labelled catalysts measured at a constant current density of 10 mA cm^{-2} in 1 M KOH with $H_2{}^{16}O$ for 30 min. The signals are normalized by the intensity of $^{16}O_2$.

The freshly prepared samples were operated at a constant current density of 10 mA cm^{-2} in 1 M KOH with $H_2{}^{18}O$ as water source for 30 min to obtain the ^{18}O-labelled Fe-NiSOH and Fe-Ni-OH samples with ^{18}O-MOOH. In this process, metal hydroxides in the samples are converted to ^{18}O-labelled metal oxyhydroxides, accompanied by O-isotope exchange.[15] As the Raman spectra shown in **Figs. S51a-b**, the vibration modes of NiOOH for the two samples are shifted by 18-20 cm^{-1} to lower frequencies compared with those of the ^{16}O-labelled samples due to the impact of oxygen mass on the vibration mode, suggesting that the Fe-NiSOH and Fe-Ni-OH electrodes are successfully labelled with ^{18}O.[15, 16] It is noted that the Ni-OH vibration mode of $Ni(OH)_2$ for the ^{18}O-labelled Fe-Ni-OH sample remains at about 460 cm^{-1}, mainly due to its incomplete reconstruction, which is consistent with the case in the ^{16}O-labelled electrolyte.

Table S1 Summary of the reconstruction results of previous OER pre-catalysts.

Pre-catalysts	Size in reconstructed direction	Reconstructed layer thicknesses	Reference
Ni_2B	8.7 μm	2-5 nm	*Energy Environ. Sci.* **2019**, 12, 684-692
Ni_2Mo_3N	2-5 μm	~3 nm	*Angew. Chem. Int. Ed.* **2020**, 59, 18036-18041
Ni nanoparticles	100-400 nm	~5 nm	*ACS Energy Lett.* **2019**, 4, 2585-2592
$NiFeB_x$	~5 μm	~2 nm	*Adv. Funct. Mater*. **2021**, 31, 2101820
Fe_2O_3 NWs	100 nm	~5 nm	*ACS Energy Lett*. **2019**, 4, 1983-1990
$NiFe_xSn$ alloy	50 nm	10-15 nm	*Adv. Sci.* **2020**, 7, 1903777
Rh-NiFe-LDH	~100 nm	10 nm	*Nano Lett*. **2020**, 20, 136-144
$NiFeO_xF_y$	~50 nm	~10 nm	*Nano Lett.* **2021**, 21, 1, 492-499
NiFe alloy	70-130 nm	< 5 nm	*Energy Environ. Sci.*, **2020**,13, 86-95
La_2NiMnO_6	~33 nm	5-8 nm	*J. Am. Chem. Soc*. **2018**, 140, 11165-11169
$Co_2(OH)Cl$	~10 nm	10 nm	*Adv. Mater*. **2019**, 31, 1805127
Ni-Fe LDH	1.2 nm	1.2 nm	*ACS Catal*. **2019**, 9, 6027-6032
F-NiFe hydroxide	100 nm	~35 nm	*Nano Lett.* **2019**, 19, 530-537

Table S2 Ni K-edge EXAFS curve fitting results for Fe-NiSOH and Fe-Ni-OH catalysts. (CN, coordination number; R, distance between absorber and backscatter atoms; σ2, Debye-Waller factor; R-factor indicates the goodness of the fit. Amplitude reduction factor S_0^2 was fixed to be 0.779, which is determined from fitting the reference sample of Ni foil. The error bounds of the structural parameters were estimated as CN ± 20 %; R ± 1 %; σ^2 ± 20 %).

Sample	Path	CN	R (Å)	σ^2	R factor
Ni foil	Ni-Ni	12 (set)	2.48	0.006	0.0007
NiSOH	Ni-O	4.3	2.02	0.009	0.0142
	Ni-S	1.6	2.26	0.009	
Fe-NiSOH	Ni-O	4.8	2.02	0.006	0.0067
	Ni-S	0.7	2.29	0.006	
Ni-OH	Ni-O	5.2	2.04	0.006	0.0054
Fe-Ni-OH	Ni-O	5.0	2.04	0.006	0.0049
Fe-NiSOH at 1.5 V	Ni-O	4.4	1.87	0.004	0.0174
Fe-Ni-OH at 1.5 V	Ni-O	5.1	2.04	0.003	0.0135

Table S3 Fe K-edge EXAFS curve fitting results for Fe-NiSOH and Fe-Ni-OH catalysts. (CN, coordination number; R, distance between absorber and backscatter atoms; σ2, Debye-Waller factor; R-factor indicates the goodness of the fit. The amplitude reduction factor S_0^2 was fixed to 0.779. Error bounds of the structural parameters were estimated as CN ± 20 %; R ± 1 %; σ^2 ± 20 %).

Sample	path	CN	R (Å)	σ^2	R factor
Fe-NiSOH	Fe-O	4.7	1.98	0.009	0.008
Fe-Ni-OH	Fe-O	4.8	1.98	0.007	0.002
Fe-NiSOH at 1.5 V	Fe-O	4.7	1.98	0.007	0.010
Fe-Ni-OH at 1.5 V	Fe-O	4.9	1.98	0.007	0.008

Table S4. Comparison of OER performance for Fe-NiSOH catalyst with recently reported transition metal (oxy)hydroxide-based pre- or reconstruced-electrocatalysts in alkaline water solution. The η_{10}, η_{100} and η_{500} are the overpotentials at current densities of 10, 100 and 500 mA cm^{-2}, respectively. * The value is calculated from the curves shown in the literatures.

Catalysts	η_{10}	η_{100}	η_{500}	Substrate	Reference
	Stability				
Fe-NiSOH	**207 mV**	**240 mV**	**260 mV**	**Ni foam**	**This work**
	100 h	**100 h**	**1100 h**		
NiFeOOH/NiFe-LDH derived from self-reconstruction	270 mV (η_{50})	290 mV	--	Ni foam	*Matter*, **2020**, *3*, 2124-2137
	24 h at 100 mA cm^{-2}				
NiGe	228 mV	350* mV	--	Ni foam	*Angew. Chem. Int. Ed.*, **2021**, *60*, 4640 – 4647
	505 h at 10 mA cm^{-2}				
(oxy) hydroxides reconstructed from FeCoCrNi	221 mV	281 mV (η_{200})	301 mV (η_{400})	Ni foam	*Nat. Commun.*, **2020**, *11*, 4066
	24 h at 10 mA cm^{-2}				
$Co_5Fe_3Cr_2$ (oxy)hydroxide	232 mV	--	--	Rotary glassy carbon electrode	*Adv. Energy Mater.*, **2021**, *11*, 2003412
	168 h at 50 mA cm^{-2}				
γ-FeOOH	286 mV	316 mV	--	Ni foam	*Adv. Mater.*, **2021**, *33*, 2005587
	24 h (10 and 50 mA cm^{-2})				
Ni-Fe-Ce-LDH	242 mV	370* mV	--	Glassy carbon electrode	*Energy Environ. Sci.*, **2020**,*13*, 2949-2956
	24 h at 10 mA cm^{-2}				
S-doped Ni/Fe (oxy)hydroxide	229 mV	281 mV	328 mV	Ni foam	*Energy Environ. Sci.*, **2020**,*13*, 3439-3446
	100 h at 100 mA cm^{-2}				
Multimetal-site oxyhydroxide	--	250 mV	--	Ni foam	*Energy Environ. Sci.*, **2020**,*13*, 2200-2208
	200 h at 100 mA cm^{-2}				
Ir/Ni(OH)$_2$	224 mV	270 mV		Ni foam	*Adv. Mater.*, **2020**, *32*, 2000872
	48 h at 10 mA cm^{-2}				
Double-Shelled Ni–Fe LDH Nanocages	246 mV (η_{20})	280* mV	--	Carbon paper	*Adv. Mater.*, **2020**, 1906432
	50 h at η_{251}				
A solid solution comprising of $MoFe_2O_4$ and $CoFe_2O_4$ nanosheets	--	240 mV	290 mV	Fe foam	*Adv. Sci.*, **2021**, *8*, 2101653
	250 mA cm^{-2} for 1000 h				
$Fe_{0.4}Co_{0.6}Se_2$ nanoframes	270 mV	--	--	Glassy carbon electrode	*Energy Environ. Sci.*, **2021**, *14*, 365
	24 h at 10 mA cm^{-2}				
NiFeCr (oxy)hydroxides	240 mV (η_{onset})	310* mV	--	Ni foam	*Energy Environ. Sci.*, **2020**,*13*, 4225-4237
	24 h at 100 mA cm^{-2}				
MOF/LDH	216 mV (η_{50})	227 mV	--	Carbon cloth	*Adv. Mater.* **2021**, *33*, 2006351
	24 h at 50, 100, and 300 mA cm^{-2}				

Table S5. Comparison of OER performance for Fe-NiSOH catalyst with other reported electrocatalysts in alkaline (simulated) seawater. The η_{10}, η_{100} and η_{500} are the overpotentials at current densities of 10, 100 and 500 mA cm^{-2}, respectively. * The value is calculated from the curves shown in the literatures.

Catalysts	η_{10}	η_{100}	η_{500}	Electrolyte	Reference
	Stability				
Fe-NiSOH	**213 mV**	**263 mV**	**311 mV**	**1 M KOH + seawater**	**This work**
	--	**110 h**	**900 h**		
B-Co_2Fe LDH	245 mV	310 mV	376 mV	1 M KOH + seawater	*Nano Energy,* **2021**, *83,* 105838
	--	100 h	100 h		
NiFe alloy@NiFeBx@ oxidized NiFeB	263 mV	320* mV	--	1 M KOH + 0.5 M NaCl	*Adv. Funct. Mater.* **2021**, *31,* 2101820
	--	328 mV	400 mV	30 wt% KOH + 0.5 M NaCl	
	--	110* h	110* h		
Fe-Ni$(OH)_2$/Ni_3S_2@NF	269 mV	310* mV	395* mV	1 M KOH + 0.5 M NaCl	*Nano Res.*, **2021**, *14*, 1149–1155
	--	27 h	--		
CoPx@FeOOH	235 mV	283 mV	337 mV	1 M KOH + seawater	*Appl. Catal. B-Environ.*, **2021**, *294,* 120256
	--	80 h	80 h		
Ni_2P-Fe_2P	--	305 mV	380* mV	1 M KOH + seawater	*Adv. Funct. Mater.*, **2021**, *31,* 2006484
	48 h (from 100 to 500 mA cm^{-2})				
NiMoN@NiFeN	--	307 mV	369 mV	1 M KOH + seawater	*Nat. Commun.*, **2019**, *10,* 5106
	--	100 h	100 h		
S-doped Ni/Fe (oxy)hydroxide	--	300 mV	398 mV	1 M KOH + seawater	*Energy Environ. Sci.*, **2020**,*13,* 3439-3446
	--	100 h	--		
Ni_3S_2/Co_3S_4	280 mV	360 mV	440 mV	1 M KOH + seawater	*Appl. Catal. B-Environ.*, **2021**, *291,* 120071
	--	100 h	--		
Co_3O_4/MnO_2	450 mV	--	--	0.5 M KOH + 0.5 M NaCl	*Appl. Catal. B-Environ.*, **2021**, *284,* 119684
	1 h at 1.94 V *vs*. RHE				

Table S6. The intensity ratio of the peaks at 553 and 463 cm^{-1} ($I_{553/463}$) for Fe-Ni-OH catalyst determined from *in-situ* Raman spectra.

Catalyst	Potential (V *vs.* RHE)	$I_{553/463}$
Fe-Ni-OH	1.125~1.365	0
	1.415	0.45
	1.465	0.61
	1.515	0.60

Table S7. The intensity ratio of the peaks at 474 and 556 cm^{-1} ($I_{474/556}$) for Fe-NiSOH catalyst determined from *in-situ* Raman spectra.

Catalyst	Potential (V *vs.* RHE)	$I_{474/556}$
Fe-NiSOH	1.365	2.05
	1.415	1.97
	1.465	1.99

Table S8. Calculated d-band, p-band center, and proportion of O 2p in SL NiOOH/FeOOH during deprotonation.

	d-band center (eV)	p-band center (eV)	Proportion of O 2p
SL NiOOH/FeOOH	-1.58	-2.23	28.20%
SL $NiOOH_{0.5}$/FeOOH	-1.75	-2.08	28.35%
SL NiOO/FeOOH	-1.78	-1.75	28.59%

References

1. B. Ravel and M. Newville, *J. Synchrotron Rad.*, 2005, **12**, 537-541.
2. G. Kresse, J. Furthmülle, *Phys. Rev. B*, 1996, **54**, 11169-11186.
3. J. P. Perdew, A. Ruzsinszky, G. I. Csonka, O. A. Vydrov, G. E. Scuseria, L. A. Constantin, X. Zhou and K. Burke, *Phys. Rev. Lett.*, 2008, **100**, 136406.
4. J. Perdew, K. Burke and M. Ernzerhof, *Phys. Rev. Lett.*, 1997, **77**, 3865-3868.
5. C. C. McCrory, S. Jung, J. C. Peters and T. F. Jaramillo, *J. Am. Chem. Soc.*, 2013, **135**, 16977-16987.
6. B. Zhang, X. Zheng, O. Voznyy, R. Comin, M. Bajdich, M. García-Melchor, L. Han, J. Xu, M. Liu, L. Zheng, F. P. G. d. Arquer, C. T. Dinh, F. Fan, M. Yuan, E. Yassitepe, N. Chen, T. Regier, P. Liu, Y. Li, P. D. Luna, A. Janmohamed, H. L. Xin, H. Yang, A. Vojvodic and E. H. Sargent, *Science*, 2016, **352**, 333–337.
7. F. Song and X. Hu, *Nat. Commun.*, 2014, **5**, 4477.
8. P. Li, X. Duan, Y. Kuang, Y. Li, G. Zhang, W. Liu and X. Sun, *Adv. Energy Mater.*, 2018, **8**, 1703341.
9. V. R. Jothi, R. Bose, H. Rajan, C. Jung and S. C. Yi, *Adv. Energy Mater.*, 2018, **8**, 1802615.
10. L. Wu, L. Yu, Q. Zhu, B. McElhenny, F. Zhang, C. Wu, X. Xing, J. Bao, S. Chen and Z. Ren, *Nano Energy*, 2021, **83**, 105838.
11. D. S. Hall, D. J. Lockwood, S. Poirier, C. Bock and B. R. MacDougall, *ACS Appl. Mater. Inter.*, 2014, **6**, 3141-3149.
12. V. Vedharathinam and G. G. Botte, *Electrochim. Acta*, 2013, **108**, 660-665.
13. B. J. Trzesniewski, O. Diaz-Morales, D. A. Vermaas, A. Longo, W. Bras, M. T. Koper and W. A. Smith, *J. Am. Chem. Soc.*, 2015, **137**, 15112-15121.
14. A. C. Garcia, T. Touzalin, C. Nieuwland, N. Perini and M. T. M. Koper, *Angew. Chem. Int. Ed. Engl.*, 2019, **58**, 12999-13003.
15. S. Lee, K. Banjac, M. Lingenfelder and X. Hu, *Angew. Chem. Int. Ed. Engl.*, 2019, **58**, 10295-10299.
16. Z. He, J. Zhang, Z. Gong, H. Lei, D. Zhou, N. Zhang, W. Mai, S. Zhao and Y. Chen, *Nat. Commun.*, 2022, **13**, 2191.